Review

Hexagonal Boron Nitride Based Photonic Quantum Technologies

Madhava Krishna Prasad [1], Mike P. C. Taverne [2,3], Chung-Che Huang [4,*], Jonathan D. Mar [1,*] and Ying-Lung Daniel Ho [2,3]

1 Joint Quantum Centre (JQC) Durham-Newcastle, School of Mathematics, Statistics and Physics, Newcastle University, Newcastle upon Tyne NE1 7RU, UK; m.krishna-prasad1@newcastle.ac.uk
2 Department of Mathematics, Physics & Electrical Engineering, Northumbria University, Newcastle upon Tyne NE1 8ST, UK; mike.taverne@northumbria.ac.uk (M.P.C.T.); daniel.ho@northumbria.ac.uk (Y.-L.D.H.)
3 Department of Electrical and Electronic Engineering, University of Bristol, Bristol BS8 1UB, UK
4 Optoelectronics Research Centre, University of Southampton, Southampton SO17 1BJ, UK
* Correspondence: cch@soton.ac.uk (C.-C.H.); jonathan.mar@newcastle.ac.uk (J.D.M.)

Abstract: Hexagonal boron nitride is rapidly gaining interest as a platform for photonic quantum technologies, due to its two-dimensional nature and its ability to host defects deep within its large band gap that may act as room-temperature single-photon emitters. In this review paper we provide an overview of (1) the structure, properties, growth and transfer of hexagonal boron nitride; (2) the creationof colour centres in hexagonal boron nitride and assignment of defects by comparison with *ab initio* calculations for applications in photonic quantum technologies; and (3) heterostructure devices for the electrical tuning and charge control of colour centres that form the basis for photonic quantum technology devices. The aim of this review is to provide readers a summary of progress in both defect engineering and device fabrication in hexagonal boron nitride based photonic quantum technologies.

Keywords: hexagonal boron nitride; quantum photonics; single-photon emitters; spin qubits; electron paramagnetic resonance; optically detected magnetic resonance; density functional theory; chemical vapour deposition; molecular beam epitaxy; van der Waals epitaxy

Citation: Prasad, M.K.; Taverne, M.P.C.; Huang, C.-C.; Mar, J.D.; Ho, Y.L.D. Hexagonal Boron Nitride Based Photonic Quantum Technologies. *Materials* **2024**, *17*, 4122. https://doi.org/10.3390/ma17164122

Academic Editor: Alexander V. Baranov

Received: 10 July 2024
Revised: 2 August 2024
Accepted: 13 August 2024
Published: 20 August 2024

Copyright: © 2024 by the authors. Licensee MDPI, Basel, Switzerland. This article is an open access article distributed under the terms and conditions of the Creative Commons Attribution (CC BY) license (https://creativecommons.org/licenses/by/4.0/).

1. Introduction

Since the advent of graphene, interest in other two-dimensional materials has dramatically increased. Hexagonal boron nitride (hBN) is a graphene-like two-dimensional material, where monolayer hBN consists of a single sheet of boron and nitrogen atoms arranged in a honeycomb structure. It has a large band gap and shows far ultraviolet light emission. Recently, defects in hBN crystals have been identified as colour centres and some of these defects are also spin active, making them suitable as single-photon emitters (SPEs) and spin qubits [1]. SPEs are essential building-blocks for the realisation of a wide range of quantum technologies, including quantum computation, quantum communications and quantum metrology.

In this review paper, we present the unique and advantageous properties of hBN SPEs which make them ideal candidates for achieving scalable photonic quantum technologies. We begin by introducing the general material (electronic and structural) properties of hBN, followed by the methods used for the growth and transfer of hBN with varying degrees of quality and crystallinity. We then provide a brief overview of the properties of hBN SPEs when compared to other candidate solid-state SPEs. We then proceed to describe the methods of controlling colour centre formation in hBN and theoretical calculations that have been conducted and correlated to experimental observations to identify their nature. Furthermore, we explore graphene/hBN based devices, which are used to tune the emission energies of hBN SPEs and control their charge states. Finally, we discuss the challenges and future perspectives on the horizon for hBN based photonic quantum technologies.

1.1. Structure of hBN

hBN consists of alternate boron and nitrogen atoms sp^2-bonded together in a honeycomb structure [2,3]. Multilayer hBN is formed by stacking layers of monolayer hBN on top of each other, held together by van der Waals forces. Due to weak interlayer forces, hBN is often used as a lubricant [4]. The lattice constant of hBN is 2.50 Å (Figure 1a) and the equilibrium interlayer spacing is 3.35 Å. Theoretical investigations using density functional theory (DFT) predicted that the preferred stacking is AA′ [5]. This comprises of switching the position of boron and nitrogen atoms in each layer, resulting in a stack where each boron (nitrogen) atom is located in-between a nitrogen (boron) atom in the adjacent layers. The preferred stacking order was confirmed to be AA′ experimentally by transmission electron microscopy (Figure 1c) [6–8].

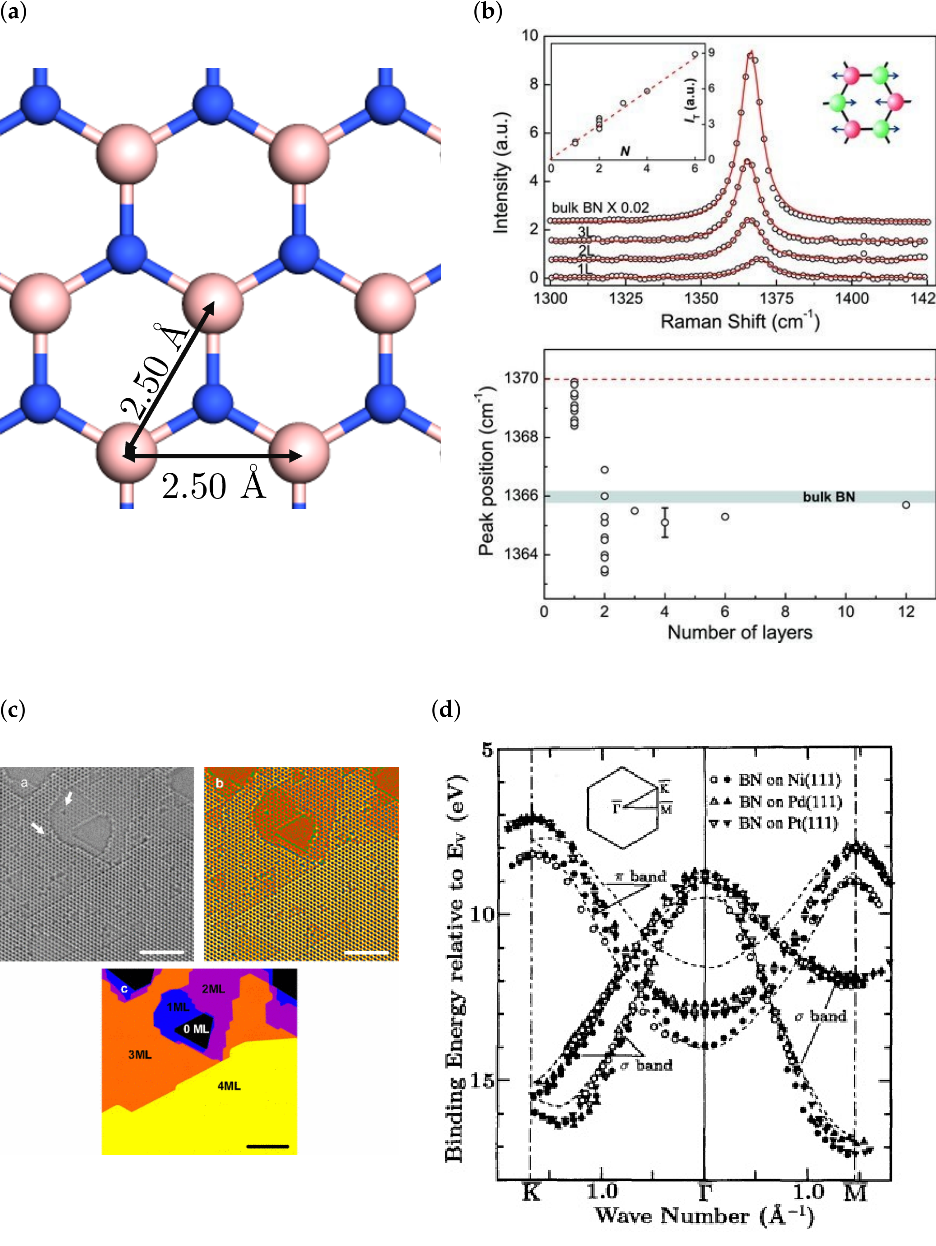

Figure 1. (**a**) Schematic of hBN with the experimental lattice parameter of 2.50 Å. (**b**) Evolution of the Raman spectrum of hBN from monolayer to multilayer hBN. (**c**) HRTEM image of hBN of different

thicknesses. By measuring the intensity profile across linear path in the image, it is possible to determine the stacking. (**d**) Experimental valence-band structures of monolayer hBN films. Reprinted Figure 1b from ref. [9] with permission from John Wiley and Sons © 2011 Wiley-VCH Verlag GmbH & Co. KGaA, Weinheim, Germany. Reprinted Figure 1c with permission from ref. [8], copyright 2009, by the American Physical Society (https://doi.org/10.1103/PhysRevB.80.155425, accessed on 9 July 2024). Reprinted Figure 1d from ref. [10], copyright 1996, with permission from Elsevier.

1.2. Electronic and Vibrational Properties of hBN

There had been a longstanding debate on the nature of the band gap of hBN, with most early DFT calculations predicting an indirect band gap [11–15] and some calculations suggesting a direct band gap [15,16]. The latter was in line with early experiments implying a direct band gap [17–19]. It has now been revealed that hBN exhibits both behaviours depending on its thickness. Monolayer hBN is a direct band gap insulator with a band gap of $\sim$6 eV, as shown by deep ultraviolet (DUV) reflectance and photoluminescence measurements in correspondence with some first principles calculations [15,20,21]. However, electron energy loss spectroscopy and two-photon spectroscopy allowed the identification of the lowest energy indirect exciton to have an energy of 5.955 eV [22,23], showing an indirect band gap with the size of the band gap being consistent with DFT calculations of bulk hBN [12,21]. The direct to indirect transition for hBN follows the behaviour of another class of two-dimensional materials called transition metal dichalcogenides (TMDs) [24] and occurs immediately from single layer to bilayer hBN [21]. This study (Ref. [21]) also found that the transition from direct to indirect band gaps was independent of the stacking order and both AA' and AB stacking exhibited the same band gap energy at the bulk limit. Angle-resolved photoemission spectroscopy (ARPES), angle-resolved ultraviolet photoemission spectroscopy (ARUPS), angle-resolved secondary electron emission spectroscopy (ARSEES) and X-ray photoelectron spectroscopy (XPS) have been employed to accurately and directly visualise the valence band structure of hBN, validating DFT calculations of the band structure, such as by confirming the location of the valence band maximum (VBM) to be at the K-point (Figure 1d) [25,26].

In terms of vibrational modes, hBN exibits two degenerate Raman active E_{2g} modes and an infrared (IR) active A_{2u} mode [27,28]. The IR mode for hBN occurs at 783 cm^{-1} and the Raman mode for bulk hBN has been observed at 1366 cm^{-1} (1370 cm^{-1} for monolayer) [9]. The intensity of the Raman peak increases with the number of layers and the peak position is usually red shifted by $\sim$4 cm^{-1} (as shown in Figure 1b) [9]. From the inset in Figure 1b, it can be seen that the intensity increases linearly with thickness, in discrete increments, and therefore by comparing the intensity of an hBN sample with known thickness and another with unknown thickness, the thickness of the sample can be determined. It is also possible to use UV-Vis absorption spectroscopy to determine the thickness of hBN, as it shows an absorption peak at $\sim$5.9 eV due to the band gap of hBN [29]. The optical absorption A, can be related to the absorption coefficient α, and the film thickness l, by $A = \alpha l$, where α has been experimentally determined [30,31].

1.3. Growth and Transfer of hBN

Highly crystalline and low defect density hBN can be grown at high pressure and high temperature using a barium boron nitride solvent (Ba-B-N) or using a Ni-Mo solvent at room temperature and pressure [32,33]. These high quality crystals can then be exfoliated onto desired substrates to obtain hBN of various of thicknesses (Figure 2a). The most common exfoliation processes are mechanical exfoliation (Scotch-tape method) and solvent assisted liquid phase exfoliation [34]. Liquid phase exfoliation can be performed by dispersing the flakes in an organic solvent followed by sonication or by dispersing in an aqueous medium, allowing for ion interacalation, followed by centrifugation [35–37].

While hBN flakes in powder form obtained from bulk hBN by exfoliation are pristine, they are usually too small for high throughput device fabrication. Furthermore, as the growth and transfer process results in a wide range of flake thicknesses, there is little

control in the vertical direction within the device stack. hBN grown from chemical vapour deposition (CVD) offers an alternative to this and allows devices to be fabricated on wafer scale [38–41].

CVD growth of hBN is often performed on a Cu or Ni catalyst using ammonia borane or borazine precursors [29,31,42]. By controlling parameters such as the catalyst, deposition temperature and pressure, the thickness of hBN can be controlled to a monolayer, as shown in Figure 2c [29,31,43]. For example, by moving from atmospheric pressure CVD (APCVD) to low pressure CVD (LPCVD), the number of layers of hBN grown was able to be reduced from a few layers to monolayer [29,31]. LPCVD can also be used to grow multilayer hBN, with a higher crystallinity than APCVD, by slowing the cooling rate [43]. It was found that the electronic properties of hBN is largely independent of the metallic substrate used as a catalyst for growth [26]. Due to the small mismatch in the lattice parameters of Ni and bulk hBN, it offers an advantage in hBN growth compared to other catalysts such as Cu [10,26]. Homoepitaxy offers a promising way to synthesise hBN by overcoming the constraint of finding a substrate with a similar lattice parameter [44]. Furthermore, controlling the surface morphology of the catalyst to achieve a greater flatness and grain size leads to the growth of hBN with fewer impurities and allotropes, such as cubic boron nitride (cBN) [38]. Wafer scale growth of hBN has also been achieved using LPCVD performed on low symmetry Cu surfaces, such as Cu (110), with large (10 cm $\times$ 10 cm) single crystal domains [45]. In contrast to the existing notions and the earlier study that single crystal hBN growth requires low symmetry crystallographic orientations of substrates, single crystal hBN was grown on Cu (111)/sapphire and theoretical calculations suggested that it was the step edges in the Cu layer that guided mono-orientated growth of hBN [46]. Other methods have used molten gold (Au) on a tungsten foil to facilitate the rotation of individual grains to align and fuse into a single crystal [39] or using a platinum, Pt (111), substrate [47]. Metal organic CVD (MOCVD) has also been used to grow hBN on the wafer scale, and overcomes the limitation on the size of hBN films imposed by the tube diameter of CVD furnaces. Wafer scale MOCVD has been demonstrated on a Ni (111) template on sapphire at 1000 °C and 30 mbar using triethylborane (TEB) and ammonia gas (NH_3) as B and N precursors, respectively [48]. First principles theoretical modelling has also been extremely useful in predicting novel precursors for MOCVD of III–V compounds, not limited to BN. An advantage of such ab initio guided methods is that it allows a deep understanding of the growth chemistry [49]. Once large areas of hBN of a desired thickness have been grown on a catalyst, it can be transferred to the desired substrate [50,51].

A common method of transfer of 2D materials, such as graphene and hBN, from the catalyst to the desired substrate is by a wet transfer process. This is outlined in Figure 3. Briefly, this involves spin coating a supporting polymer layer on top of hBN, removing hBN grown on the underside of the catalyst using a plasma, and exposing the catalyst to an etchant solution. Once the catalyst has been etched, the floating polymer/hBN film is transferred to a bath of deionised water a couple of times to remove any residual etchant and is "fished out" onto the desired substrate and dried. The polymer layer is then removed by a suitable solvent to leave behind a sheet of hBN [52]. While this is a typical process, there are a myriad of other methods that currently exist to address various issues of the transfer process to varying degrees of success [51,53,54].

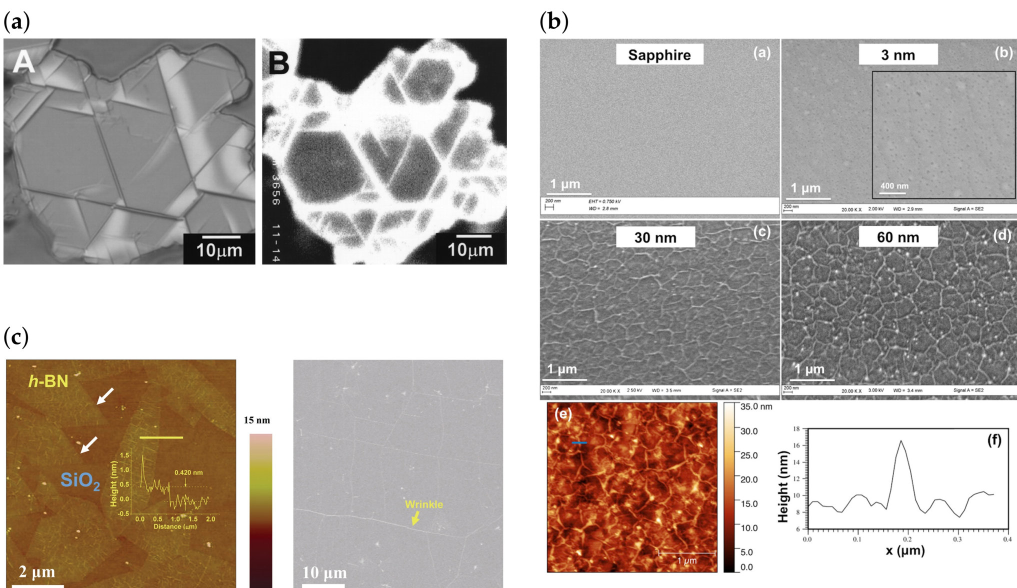

Figure 2. (**a**) Two images of hBN flakes grown at room temperature and pressure with a Ni-Mo solvent. (**A**) is a differential interference microscopy image and (**B**) is a 215 nm band cathodoluminescence image. (**b**) hBN films of various thicknesses grown on a sapphire substrate by MOVPE. (**c**) AFM image of monolayer hBN grains grown on a Cu catalyst. The step height of 0.420 nm across the line profile confirms that the hBN film is monolayer. An SEM image of a continuous monolayer is also shown, with the yellow arrow indicating a wrinkle. Figure 2a from [33]. Reprinted with permission from AAAS. Figure 2b was adapted with permission from [55]. Copyright 2016 American Chemical Society. Figure 2c was adapted with permission from [29]. Copyright 2011 American Chemical Society.

A drawback of CVD hBN is that it usually results in a higher defect density and thus a poorer quality hBN when compared to hBN flakes obtained via exfoliation. However, both of these techniques usually involve a polymer support layer which is difficult to completely remove after transfer, resulting in contamination. A possible method of removing the polymer post-transfer is by heating the transferred films in an oxygen environment beyond the decomposition temperature of the polymer [56,57].

To avoid the issues of transfer, epitaxial growth of hBN directly on the desired substrate has gained significant interest. For devices that require encapsulating graphene with hBN, van der Waals epitaxy (vdW-E) allows the synthesis of hBN directly onto graphene substrates [58,59]. Interestingly, if the hBN layer is sufficiently thick and grown on a suitable substrate, a polymer support may not be needed for transfer as the film self-delaminates from the catalyst and is not torn by the surface tension of the water. Recently, continuous and thick films have been grown on sapphire using metal-oxide vapour phase epitaxy (MOVPE) (Figure 2b) [55], with some being 1.295 µm thick [55,60], allowing for self-delamination to be used as an effective means of polymer-free transfer [61].

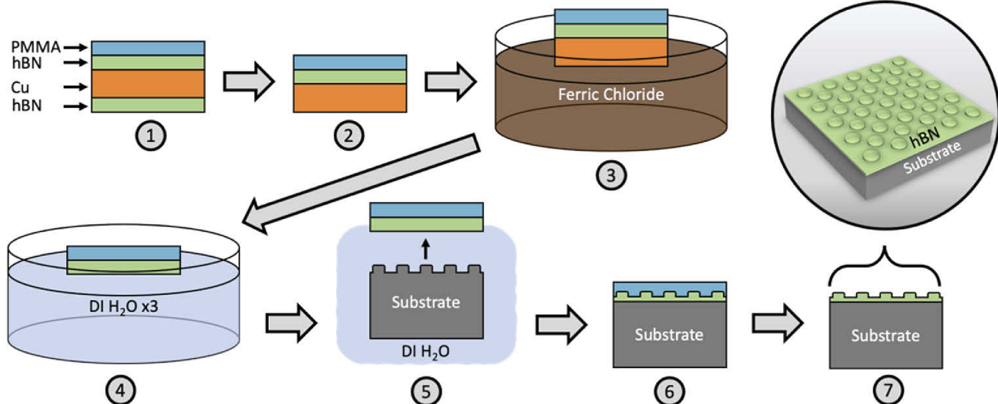

Figure 3. A typical wet transfer process for hBN from the catalyst to the desired substrate. Reprinted from [52].

1.4. SPEs in the Solid State

It is common to find point defects formed in hBN during the growth process. Point defects include vacancies, antisites, impurities and their combinations. Some of these lead to topological defects, such as Stone-Wales defects. In semiconductors and insulators, these states lead to localised states in the band gap. If a point defect leads to an occupied and unoccupied localised state in the band gap, they form a two-level system which may form the basis for a SPE. Point defects that are sources of light emission are also known as colour centres. While not all colour centres are single photon sources, in this review a particular focus is given to colour centres that are SPEs.

Before delving into SPEs in hBN, it will be useful to have an overview and comparison of the wide variety of solid-state SPEs studied so far. The mechanism by which photons are emitted depends on the type of material. In quantum dots (QDs), such as indium arsenide (InAs) and gallium nitride (GaN), and transition metal dichalcogenides (TMDs), the mode of light emission is through recombination of excitons. In both QDs and TMDs, the source of emission is through an exciton recombination. In QDs, the energy associated with this recombination is associated with the size of the QD, whereas in TMDs the single-photon emission is the result of localised excitons, potentially due to defects in the crystal—although defects in QDs can also lead to localised excitons and single photon emission [62,63]. In wide band gap semiconductors, such as diamond and silicon carbide (SiC), the source of emission is due to point defects in the crystal leading to localised states deep within the band gap. The large energy difference between the defect states involved in the transition allows these sources to be active at room temperature.

The quality of a SPE is primarily determined by the purity of its single-photon emission. This is given by the second-order correlation function, $g^{(2)}$, obtained by Hanbury Brown and Twiss (HBT) interferometry. For a SPE, $0 \leq g^{(2)} \leq 0.5$, where $g^{(2)} = 0$ for an ideal SPE. Furthermore, as some quantum cryptography protocols require two photons to be entangled, single photons must be indistinguishable. This not only requires $g^{(2)} << 0.5$ but also a narrow zero-phonon line (ZPL) with most of the emission being in the ZPL, characterised by a small phonon side band (PSB). The latter is represented by the Debye-Waller (W) factor, which is the proportion of the total emission in the ZPL. A low phonon coupling along with a narrow ZPL is highly desirable for large-scale fabrication of SPE devices. Table 1 summarises the wide range of solid-state SPEs studied so far and Figures 4 and 5 shows representative optical images, photoluminescence (PL) maps and spectra of these emitters.

1.5. SPEs in hBN

hBN being a large band gap insulator, like SiC and diamond, can possess defect states deep within its large band gap, leading to room-temperature SPEs. Furthermore, the two-dimensional nature of monolayer hBN means that the emitted light undergoes no

total internal reflection before reaching the detector and that the sources can be placed in nanometer proximity to other photonic devices (however, note that some degree of total internal reflection will be present in the case of few-layer hBN). These factors lead to a high photon-extraction efficiency, an advantage over traditional single-photon sources such as InAs QDs and diamond NV centres. SPEs in hBN have observed intensities from 4×10^6 counts/s [1,64] to 13.8×10^6 counts/s [65], making them the brightest among existing solid-state SPEs. hBN SPEs exhibit a W of 82%, implying that majority of the emission is in the ZPL [1]. The brightness can partially be attributed to a high proportion of emission into the ZPL. The purity of single-photon emission from SPEs in hBN has been measured to be $g^{(2)} = 0.077$ [65]. These properties consistently rank hBN SPEs as one of the most promising solid-state SPEs, which can be seen when compared to properties of other sources in Table 1. Furthermore, by embedding the hBN layer hosting the emitters in a multilayer hBN structure, the spectral properties can be enhanced, such as a significant narrowing of the linewidth, as seen in Figure 6a [1].

Amongst the many excellent properties of colour centres in hBN, it also hosts a wide range of defects and each of these defects have a characteristic emission spectrum (Figure 6b). The emission energies of these defects range from ultraviolet to near infrared wavelengths [1,66–68]. It is useful to categorise the visible emitters in two groups based on their lineshapes, as it is possible that they might have similar structural and/or chemical origins [67]. It was also observed that irrespective of the category of visible light emitter, the phonon sideband (PSB) is separated from its corresponding ZPL by about $\sim$160 $\pm$ 5 meV. However, a caveat is that no SPEs emitting at telecommunications wavelengths have been discovered yet, giving hBN SPEs a significant disadvantage when compared to InAs QDs and TMDs when considering the compatibility of these sources with existing silicon technologies [69,70].

Table 1. Properties of existing solid-state single photon emitters, excluding hBN. RT: Room Temperature, W: Debye-Waller factor. The following abbreviations are used for emitters: NV: Nitrogen-Vacancy, SiV: Silicon-Vacancy and CNT: Carbon Nanotube.

Source	Bulk or 2D	T	Brightness (Counts/s)	Purity ($g^{(2)}$)	W (%)	Emission Range (nm)
Diamond NV^-	Bulk	RT	$\sim 1 \times 10^6$ [71]	0.1–0.3 [71]	4–20 [72,73]	637 [71,74,75]
Diamond SiV	Bulk	RT	$\sim$1–5 $\times 10^6$ [76,77]	<0.2 [76,77]	70–97 [76]	738 [73,76,77], 726.5 and 740.8 [78]
InAs QDs	Bulk	up to 80 K [79]	$\sim 10^4$ [80,81],	0.00044 [69], 0.006 [62]		1500 [69], 1550 [79]
SiC	Bulk	RT	$\sim 2 \times 10^6$ [82]	<0.13 [82,83]	8–40 [84,85]	427–745 [86], 858, [84] 862, 917 [85,87], 1033–1137 [88], 1540 [89], 726.5 and 740.8 [78]
TMDs	2D	4 K	0.37×10^6 [90]	<0.21 [90]	0.01–0.64 [91]	708–757 [63], 1080–1550 [70]
CNTs	Nanotubes	RT	$\sim 10^4$ [92,93]	0.01 [92], 0.04–0.39 [94]		980 and 1120 [95], 975 and 1137 [96], 991 and 1158 [97], 1140–1580 [92]
GaN QDs	Bulk	RT	$\sim 10^7$ [98]	0.01–0.3 [99–101]		270 nm–290 [98,102], 338 nm [100], 1120 nm, 1225 nm, and 1300 nm [101]

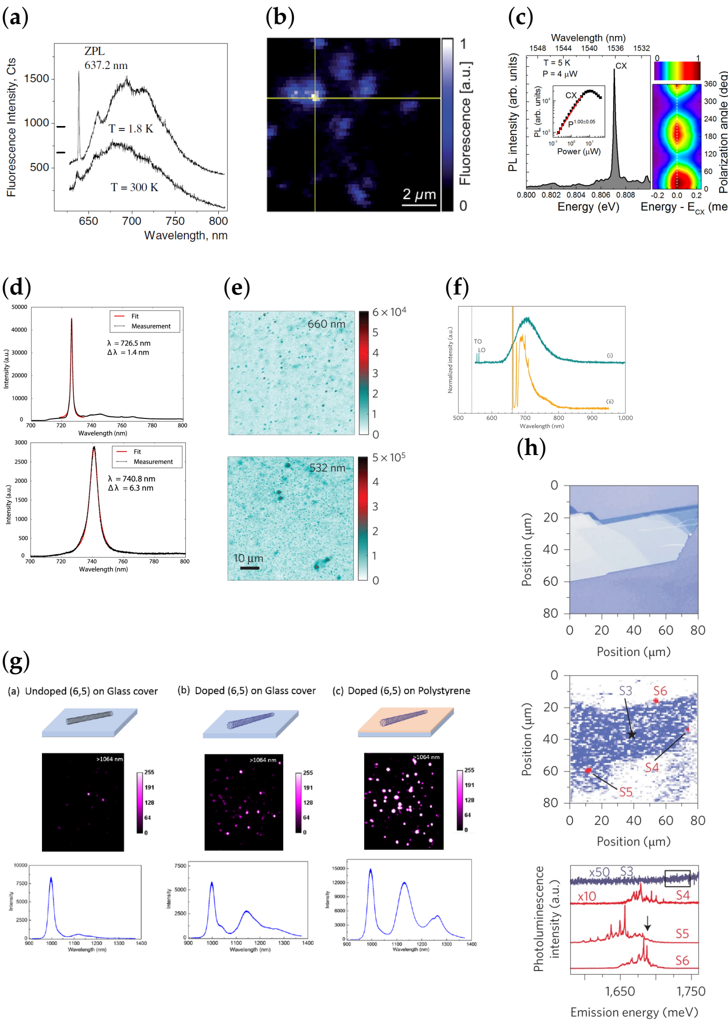

Figure 4. (**a**) Spectra of the NV^{-} centre in diamond. (**b**) Confocal PL map of NV centres embedded in a solid immersion lens. (**c**) µPL spectra and polarisation resolved measurement of InAs/InP quantum dots. (**d**) PL spectra of SiV centre in diamond. (**e**) Confocal PL map of colour centres in SiC. (**f**) Typical spectra of defects in SiC which are SPEs. Here the same SPE has been excited with a 532 nm (i) and 600 nm (ii) source. (**g**) Wide-field PL maps (50 µm × 50 µm) of unfunctionalised and functionalised (by 3,5-dichlorobenzene diazonium (Cl_2-D_z)) single-walled carbon nanotubes (SWCNTs) on glass and doped SWCNTs on polystyrene and their respective ensemble PL spectra. (**h**) (**Top**) An image of a thick WSe_2 flake obtained using an optical microscope. (**Middle**) Micro-photoluminescence scan of the flake, showing intensity in the range 1.71–1.75 eV. (**Bottom**) Emission spectra found at specific locations on the edges (S4–S6). These locations are indicated in (**Middle**) with a red contrast contour plot of the intensity of the PL signal observed at E = 1.687 eV (E indicated by the arrow). Figure 4a reprinted with permission from [75]. © 2006 WILEY-VCH Verlag GmbH & Co. KGaA, Weinheim, Germany. Figure 4b reprinted from [71] and used under Creative Commons Attribution-NonCommercial-ShareAlike 3.0 Unported (http://creativecommons.org/licenses/by-nc-sa/3.0/, accessed on 9 July 2024) license. Figure 4c reprinted from [79], with the permission of AIP Publishing. Figure 4d adapted from [78] (plots re-arranged) and used under Creative Commons Attribution 3.0 license (https://creativecommons.org/licenses/by/3.0/, accessed on 9 July 2024). Figure 4e,f adapted from [82] with permission from Springer Nature (https://doi.org/10.1038/nmat3806, accessed on 9 July 2024). Figure 4g reproduced from [92] with permission from Springer Nature (https://doi.org/10.1038/nphoton.2017.119, accessed on 9 July 2024). Figure 4h reproduced from [63] with permission from Springer Nature (https://doi.org/10.1038/nnano.2015.67, accessed on 9 July 2024).

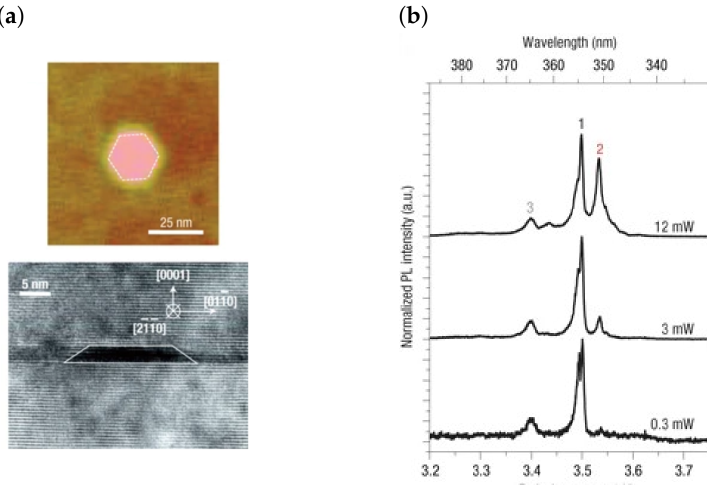

Figure 5. (**a**) Atomic force microscopy (AFM) of a GaN QD that is uncovered and a cross-sectional TEM of a covered GaN/AlN QD. (**b**) PL spectra of a GaN/AlN QD obtained at different excitation powers. Reproduced from [99] with permission from Springer Nature (https://doi.org/10.1038/nmat1763, accessed on 9 July 2024).

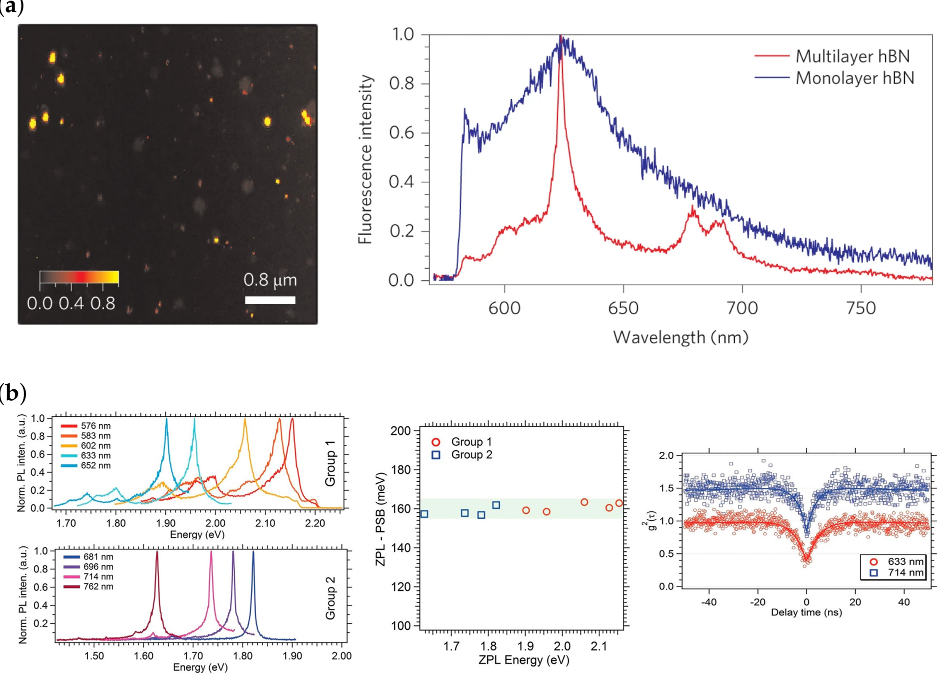

Figure 6. (**a**) (**Left**) Confocal PL map of colour centres in hBN. A subset of these are SPEs. (**Right**) Representative spectra of a visible light SPE in multilayer and monolayer hBN. Emitters have a significantly narrower linewidth when embedded in multilayer hBN. (**b**) (**Left**) Wide range of spectra obtained from different emitters. Due to their similar lineshapes, it is common to divide these spectra into two groups. (**Centre**) shows that both categories of emitters have PSBs a similar distance away from the ZPL. (**Right**) $g^{(2)}$ measurements confirming antibunching from emitters in both groups. Figure 6a reproduced from [1] with permission from Springer Nature (https://doi.org/10.1038/nnano.2015.242, accessed on 9 July 2024). Figure 6b Adapted with permission from [67]. Copyright 2016 American Chemical Society.

2. Colour Centres in hBN

As mentioned earlier, due to the wide range of defects present, hBN hosts SPEs emitting within a wide wavelength range, from UV to near IR. Significant effort has been invested in controlling the type and location of defects in hBN, a crucial step in creating arrays of emitters for use in scalable photonic quantum technologies based on hBN SPEs. The ultimate goal is to deterministically fabricate a specific type of defect at a pre-determined location in a high-quality crystal.

Defects are naturally formed during the growth process of hBN. Flakes grown using high pressure and high temperature (HPHT) have the lowest defect densities [19,32,33]. Hence, they are a suitable platform for the deterministic fabrication of defects. However, flakes obtained from exfoliated layers from a larger bulk crystal have no deterministic control over the thickness or lateral size of the exfoliated flakes. Hence, high throughput fabrication of devices is unsuitable using this source of hBN. hBN obtained from CVD allows wafer scale fabrication and thickness control of devices, however they have a high density of defects and the transfer process from the CVD catalyst to a suitable substrate can lead to significant contamination [56,103].

2.1. Creation of Colour Centres in hBN

2.1.1. Annealing

Despite the natural occurence of defects, some of which are colour centres in hBN, they are usually unstable [1]. In order to improve the stability of these colour centres, and also create a larger number of colour centres, annealing in an Ar flow at 850 °C is employed [1,67,104]. It was found the defect densities increased with annealing temperature, suggesting that the defect was vacancy related, and that they were likely to be neutrally charged as they were unaffected by annealing in hydrogen, oxygen and ammonia environments, which are known to change the charge states of defects [67]. Beyond argon, exfoliated flakes annealed in a CH_4 environment at 1000 °C showed a nine-fold increase in the density of emitters when compared to argon annealing at 1000 °C [105]. Purely annealing seems to produce emitters with a wide range of emission wavelengths, from 565 nm to 775 nm when annealed in an argon environment at 850 °C [67] and from 520 nm to 720 nm (with most emitters at 540 nm) with CH_4 annealing at 1000 °C [105]. The current standard of determining the emitter density is an areal density, which is calculated by dividing the total number of emitters in a flake by the total area of the flake [105,106]. Unlike in Ar annealing, which resulted in a low areal density of emitters (0.009 emitters/μm^2) concentrated around flake edges, annealing of hBN flakes in an O_2 flow led to 0.327 emitters/μm^2 and the defects seemed to be uniformly distributed throughout the flake [107]. While annealing can stabilise and create new emitters, it can also lead to the loss of some existing colour centres. For example, blue emitters (ZPL at 436 nm) fabricated in carbon-doped hBN flakes were stable under annealing in 1 Torr of Ar for 30 min, the standard annealing recipe to generate and stabilise emitters, for up to 800 °C, but disappeared when the annealing temperature was raised to 1000 °C and was followed by the creation of new emitters with a distribution of ZPL energies [108].

2.1.2. Ion Implantation, Electron Beam and Laser Pulse Irradiation

In hBN crystals with low defect densities, ion and electron beam irradiation is effective in creating defects [65,67,104,109–114]. Ion beam irradiation usually requires an additional annealing process to stabilise the emitters [104,110]. A study exploring ion beam implantation performed using B, N, BN, Si and O ions on exfoliated hBN flakes followed by annealing in argon at 850 °C all produced defects with similar PL spectra consisting of a peak around 600 nm with a phonon side band 160 meV from the ZPL [104]. In the same study, a reference sample that was only annealed in argon without any implantation also produced emitters with similar characteristic spectra, albeit at a lower density, suggesting that the defects created had similar structures. Furthermore, after annealing, the emitters were mostly found on the edges of the flakes, indicating the role of strain in defect forma-

tion. In a different investigation, ion implantation done using He and N atoms followed by argon annealing increased the emitter density by orders of magnitude, however the defects were still predominantly located on flake edges [110]. However, unlike in the previous study, the spectral characteristics of the colour centres are spread over a broad range, with ZPLs from 569 nm to 697 nm. In Figure 7a, we can see that the problem of spatial localisation can be addressed by the use of a focused ion beam (FIB) to achieve precise localisation of defects [112,115–118]. Defect creation using FIB involves the breaking of the B-N bond using high energy ions, leaving behind vacancies. By the use of Xe^+ [115], and N and O ions [112], the negatively charged boron vacancy was able to be deterministically generated, having a ZPL at approximately 820 nm.

Similar to ion implantation, electron beam irradiation has been a popular way to controllably generate emitters [67,104,111]. The irradiation is performed at energies much lower than threshold at which electron beam induced etching of hBN occurs. Unlike ion implantation, electron beam irradiation allows both the creation and activation of emitters in a single step, since no additional annealing process is required to stabilise emitters [67,104,111]. In terms of the types of emitters produced, exposing a large region, such as a whole flake, to irradiation, results in a wide range of defects [104], although in some cases some emitter types may occur at a higher frequency than others [67] and in all cases are predominantly located at flake edges. An approach that was successful in also creating emitters in flatter regions of the hBN flake was to increase the energy of the incident electron from the typical values of 15 keV [67,104] to a few MeV [119]. Localised doses of electron beam irradiation have been successful in the creation of spectrally and spatially well-defined defects [111,120,121]. In Figure 7b, we can see that by focusing the beam radius to around 33 nm at low energies of 15 keV, colour centres emitting at 435 nm were able to be reproducibly generated [111,120]. However, while such a process can allow control over defect creation, the yield of SPEs was quite low, as it was more likely to form an ensemble of defects than single emitters [120]. Although there are no studies on the site-controlled creation of boron vacancies, high energy (2 MeV) electron beam irradiation has been used to create boron vacancies in hBN flakes [121].

Femtosecond pulsed laser irradiation has also been a reliable technique to generate emitter arrays on demand [122–124]. The laser pulse can be used to induce a hole in the hBN, around which colour centres form. It was shown that vacuum annealing also resulted in the conversion of the defects into paramagnetic colour centres and that the defect density around the ablation site could be controlled by manipulating the pulse energy [122], leading to the possibility of optimising the pulse energy to produce single emitters [123,124]. It was shown that for pulse energies of 38 nJ and 46 nJ, there was 100% yield of SPEs [123]. A reduction in the laser pulse energy not only reduced the density of emitters but their ZPL energy distributions as well, with a lower pulse energy generally resulting in fewer distinct types of PL spectra [123]. It is also interesting to note the role of annealing in SPE creation by laser writing is not conclusive, with some reporting that UV/ozone annealing is crucial for the activation of defects [122,123] and others reporting the contrary [124]. In each of these studies, the ZPL energies were distributed in the visible light range, from 550 nm to 800 nm [122]. The negatively charged boron vacancy can also be created reproducibly using laser writing using 1 µJ pulses and less than 200 pulses [125].

Building on the above irradiation methods, neutron irradiation also resulted in the creation of negatively charged boron vacancies [126]. Like electron irradiation and unlike ion implantation, annealing was not performed to activate or stabilise the defects.

2.1.3. Chemical and Plasma Etching

Etching of hBN in reactive environments is an effective way of creating colour centres. Plasma etching in O_2 and subsequent annealing in argon, a step that was found to be necessary in order to have bright and stable emitters, led to the formation of emitters spanning the visible light wavelength range [127]. Other combinations of plasma etching and annealing include CH_4 and H_2 plasma etching followed by annealing in air at 850 °C

and Ar plasma etching and Ar annealing at 850 °C or air annealing at 750 °C [68,107]. Ar plasma etching and annealing at 850 °C led to an 8-fold increase in emitter density [68]. While plasma etching leads to emitters distributed randomly at flake edges or cracks in the lateral directions, the emitters were observed to form at the surface of the flakes [128]. Furthermore, by optimising the layer-by-layer etching process of hBN flakes, the emitter could be localised in the vertical direction. In addition to undirected plasma etching, highly directional plasma etching using reactive ion etching (RIE) with oxygen ions and subsequent annealing at 850 °C in nitrogen (N_2) allowed the production of emitter densities up to 0.028 μm^2, using irradiation energies of 240 eV and irradiation times of up to 1000 s [106].

Chemical etching has been performed using both peroxymonosulfuric acid (H_2O_2:H_2SO_4) and additional (H_3PO_4 + H_2SO_4) solutions [110]. Process 1 involved etching in a 3:6 solution of H_2O_2:H_2SO_4 for 2 h at 135 °C. The second process involved performing Process 1 for 20 min followed by etching in a 1:8 solution of H_3PO_4:H_2SO_4. After both processes, annealing at 850 °C in Ar was performed. The emitter density due to Process 1 was 0.09 emitters/μm^2, however it dramatically increased to 0.57 when Process 2 was used.

2.1.4. CVD hBN

As mentioned earlier, CVD hBN allows wafer scale production of hBN quantum emitter based devices and vertical control over emitter localisation as the thickness of the hBN can be controlled during growth. The CVD growth process leads naturally to the existence of a high density of defects throughout the film, with relatively low distributions of ZPL energies [129]. While the natural existence of a high density of emitters is advantageous, the lack of control over the defect location and type is a limitation. Therefore, significant effort has been invested in the development of specific emitter types during growth. A study focused on using LPCVD growth using ammonia borane (BH3NH3) as a precursor in a quartz tube furnace, at a temperature of 1030 °C, with Ar/H_2 as a carrier gas producing a uniform, few layer hBN film when a very low partial pressue of H_2 (0.05%) and gas flow rate (50 sccm) [130] is used. The emitter density was uniform throughout the sample and not localised to areas of high strain (edges or wrinkles), and had a narrow distribution of ZPL wavelengths. It was found that more than 85% of the emitters exhibited ZPL wavelengths in the 580 ± 10 nm spectral range, and up to 56% in the 580 ± 5 nm range. Furthermore, the PSB of these emitters were almost always located 165 meV below the ZPL, suggesting a similar structure for all the defects. It was also noted that a high emitter density, an overall density of 2.2 emitters/μm^2 and a single emitter density of 0.84 emitters/μm^2 was achieved without the need for annealing, a marked improved over 0.04 emitters/μm^2 [129]. Efforts have also been made to spatially localise emitters during the growth process. It was found that LPCVD growth of hBN on Ni led to preferential formation of the brightest emitters on Ni (100) grains [131]. In most CVD grown hBN, the spectral window in which the emitters occur is limited to 580 ± 10 nm, with practically no emitters emitting beyond 600 nm [129–131]. It was also found that controlling the diffusion of boron through the Cu catalyst offered a mode of controlling the type of emitters formed during CVD growth of hBN [132]. Using a process labelled as 'backside boron gettering (BBG)', hBN growth was controlled by stacking the oxidised Cu catalyst on a Ni substrate rather than a quartz substrate. As the solubility of B atoms is higher in Ni than Cu, the B atoms predominantly diffuse through the Ni substrate than Cu, leading to a significantly slower growth rate of hBN than when compared to when oxidised Cu was placed on a quartz substrate. Analysis of the SPEs generated during hBN synthesis revealed that hBN grown using BBG hosted 87% of its emitters in the 550 nm to 600 nm region, while hBN grown on oxidised Cu on quartz led to the formation of 87% of its color centres in the 600–650 nm region. Standard growth of unoxidised Cu on quartz resulted in all the emitters being in the 600-650 nm window. While this last result is contradictory to [130,131], the difference in the dominant spectral window for emitter creation can be attributed to the growth in [132] being performed in atmospheric pressue rather than low pressure, an effect that is commonly observed during hBN growth processes [133]. Controlling

boron diffusion also served as a useful way to control emitter densities as emitters grown using BBG, oxidised Cu on quartz and standard Cu on quartz resulted in SPE densities of 1.00 emitters/μm^2, 1.66 emitters/μm^2 and 3.11 emitters/μm^2, respectively.

2.1.5. Strain Activation

From the ubiquitous observation of emitters concentrated around flake edges, it became apparent that strain played a role in the formation of defects. This has inspired attempts at exploiting strain to localise emitter creation. One study etched SiO_2 nanopillars of various diameters and directly grew hBN using CVD on these nanopillars (Figure 7c), and it was found that when the pillar diameters were 250 nm and 650 nm high, there was an 80% yield of SPEs at the pillar site [134]. Furthermore, the distribution of ZPLs was between 559 nm and 639 nm, a much smaller distribution in ZPL wavelengths than when annealing alone or when using large-area electron/ion beam irradiation. An important note is that no post-growth annealing was performed on the sample to increase/stabilise emitters. In a different investigation, hBN flakes were exfoliated onto silica microspheres to introduce strain fields and intense fluorescence was observed from 560 nm to 780 nm [135]. In the latter work, emitters were found only in the region of hBN directly lying on the microspheres and these emitters were active before and after annealing in Ar at 850 °C. A near-deterministic activation of defects was also observed when CVD hBN was transferred onto an array SiO_2 micropillars [136]. An average of 2 emitters per pillar was found on pillars with a diameter of 75 nm and height of 155 nm, with some hosting SPEs. Like the first investigation [134], the emitter activation did not require annealing. The role of strain was confirmed by a repetition of [136], albeit for pillar diameters ranging from 0.6 μm to 2 μm and even a bullseye cavity and an optimised transfer process of the CVD hBN. The brightest emitters were observed at the location of the pillars and cavities, emphasising the role of strain in defect activation [52].

2.1.6. Other Methods

Molecular beam epitaxy (MBE) of hBN is an alternative to CVD when growing large-area hBN. In a study investigating the role of carbon in the formation of SPEs in hBN, MBE of hBN on sapphire was performed by placing the boron source in a carbon crucible. Sharp spectral lines were observed which did not exist during standard MBE of hBN without the carbon crucible [137]. As the carbon crucible showed sidewall etching, it suggested that carbon was present in gaseous phase during growth and the emergence of the new spectral lines could be strongly attributed to the carbon doping of hBN. This conclusion was supported by the observation of a high emitter density when other methods of increasing carbon incorporation into hBN was employed. These methods include varying the flow rates of triethylboron (TEB) during metal organic vapor phase epitaxy (MOVPE) growth of hBN, known to systematically alter the concentrations of carbon present, exploring the possibility of carbon incorporation from the substrate by performing high-temperature MBE on different orientations of SiC and converting highly orientated pyrolytic graphite (HOPG) into hBN. An increase in emitter intensities and densities with increasing TEB flow rates, variations in SiC orientation during MBE growth and conversion of HOPG into hBN offers strong support to the correlation between carbon doping and SPE creation. Furthermore, the PL spectra observed using each method of growth was mostly similar, suggesting similar defect structures.

An interesting technique for spatially localising emitters was using atomic force microscopy (AFM) to perform nanoindentation in exfoliated hBN flakes. In these samples, there was a 32% yield in SPEs for an indent of 400 nm in size. The ZPL wavelengths produced using this method can be categorised into three classes: 582 $\pm$ 6 nm, 602 $\pm$ 9 nm, and 633 $\pm$ 5 nm. More than 80% of the SPEs show ZPLs being positioned in the 580 nm and 602 nm groups [138].

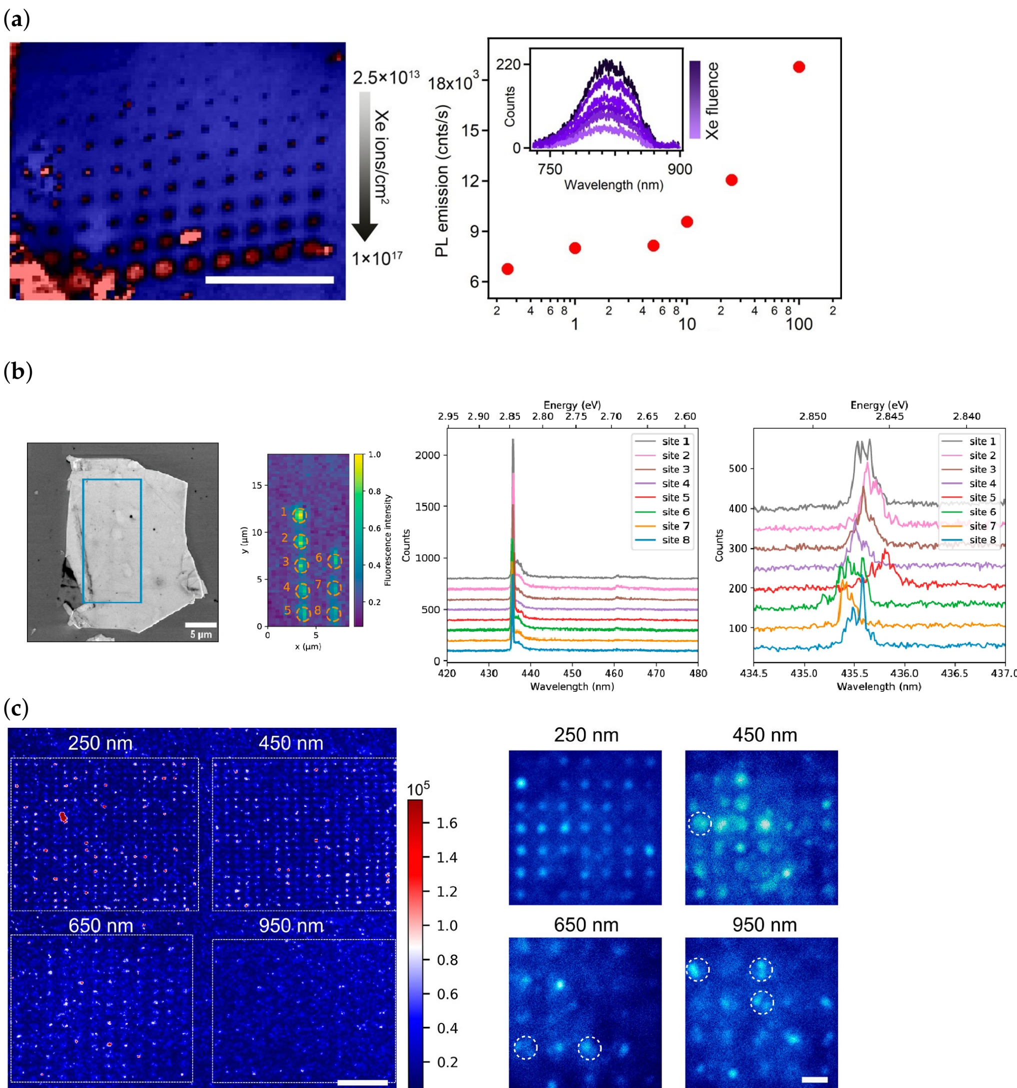

Figure 7. (**a**) (**Left**) Negatively charged boron vacancies observed in a confocal scan, created using a focused ion beam of Xe^+ ions, with the fluence of ions increasing with each row and constant across each row. Scale bar 20 µm. (**Right**) Variation of PL intensity with Xe^+ fluence. The inset shows a representative PL spectrum for each fluence. (**b**) (**Left-most**) Image taken using a scanning electron microscope (SEM) of a hBN flake, with the blue rectangle indicating the region irradiated with an electron beam. (**Centre-left**) Confocal map of rectangle zone. (**Centre-right**) and (**Right**) are PL spectra at each exposed site taken at low temperature (5 K) at two different spectral resolutions, showing a reproducible 0.7 nm spectral linewidth. (**c**) (**Left**) Confocal PL intensity maps of strain induced colour centres in hBN. The hBN was directly grown using CVD onto the nanopillars. The pillar diameters are 250, 450, 650, and 950 nm and the scale bar is 10 µm. The unit for the intensity is photon counts/s. (**Right**) Wide-field images of each pillar array with hBN deposited on it. White circles indicate pillars with multiple emitters. The scale bar is 2 µm. Figure 7a adapted with permission from [115]. Copyright 2020 American Chemical Society. Figure 7b reprinted from [111] and used under a Creative Commons Attribution 4.0 International (https://creativecommons.org/licenses/by/4.0/, accessed on 9 July 2024) license. Figure 7c adapted with permission from [134]. Copyright 2021 American Chemical Society.

2.2. Defect Assignment

In order to understand the nature of defects observed in experiment, comparisons with theoretical calculations need to be made. The most common method of calculating the electronic structure of defects and subsequently the structure for comparison with experiment is density functional theory (DFT). In DFT, the derived values can vary significantly between choice of exchange-correlation functional. For example, the hBN band gap obtained using the Perdew-Wang (PW91) generalised gradient functional (GGA) is 4.6 eV [15,139], which is much smaller than the value of 6.47 eV obtained using Heyd-Scuseria-Ernzerhof (HSE), screened exchange functionals [21,140]. Unless explicitly stated, all DFT derived values have been calculated using HSE functionals as it is the current de facto standard for calculating these values.

A range of defects have been studied theoretically, such as vacancies, anitsites, impurities, complexes of antisites and impurities with vacancies, and Stone-Wales defects, to name a few [1,141,142]. In the following discussion regarding defects, the following notation is used to describe defects. The species being replaced is indicated as a subscript of the species that it is being substituted for. For example, a nitrogen vacancy is represented by V_N, as a vacancy is substituting a single nitrogen atom. Similarly, the antisite nitrogen vacancy complex is symbolically written as N_BV_N, as the nitrogen atom is replacing replacing the boron atom (N_B) and is coupled to a nitrogen vacancy (V_N). Values derived from DFT include but are not limited to theoretical ZPLs, Huang-Rhys factors, S, (which show the degree of phonon coupling and is related to W by $W = e^{-S}$) and defect formation energies.

The N_BV_N defect was one of the first candidate defects suggested to be a SPE [1]. Some calculations predicted a planar defect geometry (Figure 8a) [1,141,143], and others found the ground state configuration to involve an out-of-plane displacement of the nitrogen atom [144]. The defect is also expected to have a spin doublet ground state and therefore has gained interest as a spin qubit [141,143]. The electronic structure of the neutrally charged defect involves three defect states in both spin channels within the band gap (2 occupied in the spin majority and 1 occupied in the minority spin channel), Figure 8b [1,143]. The PBE calculated ZPL transition for this defect has an energy of 2.12 eV, which is in the range observed experimentally, and S is calculated to be 0.66 [141] and the HSE derived ZPL is 2.05 eV [145]. The large S makes the defect less likely to be a candidate as it predicts a large phonon coupling, something not observed in experiment [141].

A candidate similar in nature to N_BV_N is the carbon impurity and nitrogen vacancy complex, C_BV_N. Early work on this defect suggested that the defect had a triplet ground state with C_{2v} geometry, i.e., the carbon atom was in plane [141,146]. Like N_BV_N, C_BV_N has three states in the band gap of each spin channel, with two occupied states in the majority spin channel. The transition energy of this defect is calculated to be 2 eV with $S = 1.50$ [147], which is very close to the S of 1.45 obtained from some experimentally obtained PL spectra [137], making it a suitable candidate for visible light emitters centered around 600 nm. From Figure 8f, it can be seen that the theoretical and experimental spectra agree well. However, it was later found that the true ground state of the C_BV_N defect is the singlet ground state, with an out-of-plane distortion of the carbon atom giving it C_{1h} symmetry [144,148,149]. While the ZPL energy associated with this defect is 2.08 eV, putting it within the observed ZPL energy range, it was shown that the excited state has a significant lattice distortion when compared to the ground state, implying large phonon coupling and contradicting observations of the ZPL contributing to the majority of the emission [148,149]. This finding makes it less likely that the transition is due to this defect.

Beyond the visible light emitters, the nature of the UV light emitters has gained significant interest. Some studies suggested that the source of this emission is a topological defect, specifically the Stone-Wales defect which leads to two six-member rings transforming into a five-member and seven-member ring [150]. The Stone-Wales defect is formed by a 90° rotation about the axis perpendicular to the hBN sheet which automatically introduces a nitrogen antisite and a boron antisite, creating a nitrogen-nitrogen and boron-boron bond. It was found from first principles calculations using DFT that the N-N bond leads to a

level that is 0.44 eV from the valence band maximum and the B-B bond leads to an energy level 0.4 eV below the conduction band [142]. The lowest defect state in the band gap is fully occupied, leading to a singlet ground state. The calculated ZPL energy and simulated S of this defect is 4.08 eV and 2, respectively, in good agreement with spectra observed in [151,152]. Despite the excellent agreement between theoretical and experimental spectra, the formation energy of the Stone-Wales defect is relatively high at 7.2 eV suggesting that the defect should occur in low abundance [142]. However, regions of high strain in the hBN crystal could lower the formation energy of such defects, leading to a greater concentration [142]. In Figure 8h, we can see the structure, simulated spectra and band structure of a Stone-Wales defect.

A competing theory for the nature of the 4.1 eV emission is the carbon dimer. It has been seen experimentaly that the intensity of the 4.1 eV peak increases with carbon doping [153,154], indicating that the nature of the defect is carbon related. The carbon dimer is formed by substituting neighbouring B and N atoms to form C_BC_N. The formation energy of the neutral charge state of this defect is 2.2 eV [155], 5 eV less than the Stone-Wales defect, making it significantly more likely to form. The calculated values of the ZPL and S for this defect range from 4.31 eV [155] to 4.36 [156] and 1.37 [156] to 2 [155], respectively. Like the Stone-Wales defect, the carbon dimer has a planar C_{2v} structure [156]. The carbon dimer can be thought of as a combination of two defects, the substitutional carbon on the boron site and nitrogen site. Both impurity defects lead to a single defect state in each spin channel, with spin splitting leading to the majority spin channel having a lower energy [157]. The C_B defect creates a donor state below the conduction band and the C_N creates an acceptor state below the conduction band. The formation of the C_BC_N defect leads to a combination of the electronic structures of C_B and C_N, with the highest occupied molecular orbital (HOMO) and the lowest unoccupied molecular orbital (LUMO) levels residing above the valence band and conduction band a similar energy difference from the band edges for isolated C_B and C_N. As seen in Figure 8e, the fully occupied HOMO and LUMO leads to a singlet ground state and loss of spin splitting existing in the isolated components of the dimer. The excellent spectral agreement between theory and experiment, and the low formation energies makes the carbon dimer one of the most likely candidate defects for UV light emission. It was also discovered that every donor-acceptor pair C_BC_N present in a carbon cluster led to a reduction in formation energy of the cluster. This results in carbon clusters being increasingly stabilised when there is an equal number of C_B and C_N, with the stabilisation energy of the six-member carbon ring (three C_BC_N pairs in a ring) being the largest. The stabilisation can be attributed to the formation of a delocalised π electron orbital similar to the benzene molecule, leading to a reduction in the kinetic energy of electrons. Among larger carbon clusters, carbon trimers, C_2C_N and C_2C_B, have been calculated to have spectral characteristics that show a striking resemblance to the visible light emitters, Figure 8d, i.e., a 1.6 eV ZPL and a PSB 160 meV from the ZPL [158,159], although some calculations suggest that C_2C_B has a ZPL energy of 1.36 eV [160]. The reason for this discrepancy is unknown.

Out of the many candidate defects, the negatively charged boron vacancy, V_B^- is the only defect that has been conclusively identified. The neutral boron vacancy, V_B, has a C_{2V} geometry due to a Jahn-Teller distortion lowering its symmetry from D_{3h} [161]. The formation energy of the neutral defect is 7.65 eV using HSE functionals, where such a high formation energy is typical for vacancies [161]. Previous studies [162] indicate V_B is a triple acceptor, and a single acceptor level is located at 1.4 eV [161–163] and the double acceptor level has been estimated to be in the range of 3.9 eV [161,162]. The triple acceptor level is very close to the conduction band and is not found to be stable [162]. The defect states of V_B are largely derived from valence-band orbitals. There are three defect levels in each spin channel, with two (one) occupied and one (two) unoccupied states in the spin majority (minority) channel [161]. The negatively charged boron vacancy, shown in Figure 8c, is a spin triplet with D_{3h} symmetry [161,162,164] and zero field splitting causes the triplet degeneracy to be fully lifted [164]. Electron paramagnetic resonance (EPR) and

optically detected magnetic resonance (ODMR) measurements of defects induced in hBN flakes by neutron irradiation, which emitted at 800 nm, led to the conclusive assignment of these emitters as V_B^- [126]. This was later further confirmed by DFT calculations which found that the V_B^- has a ZPL transition at 1.65 eV (765 nm) and a large S of 3.5, implying a significant phonon coupling, unlike other defects [164].

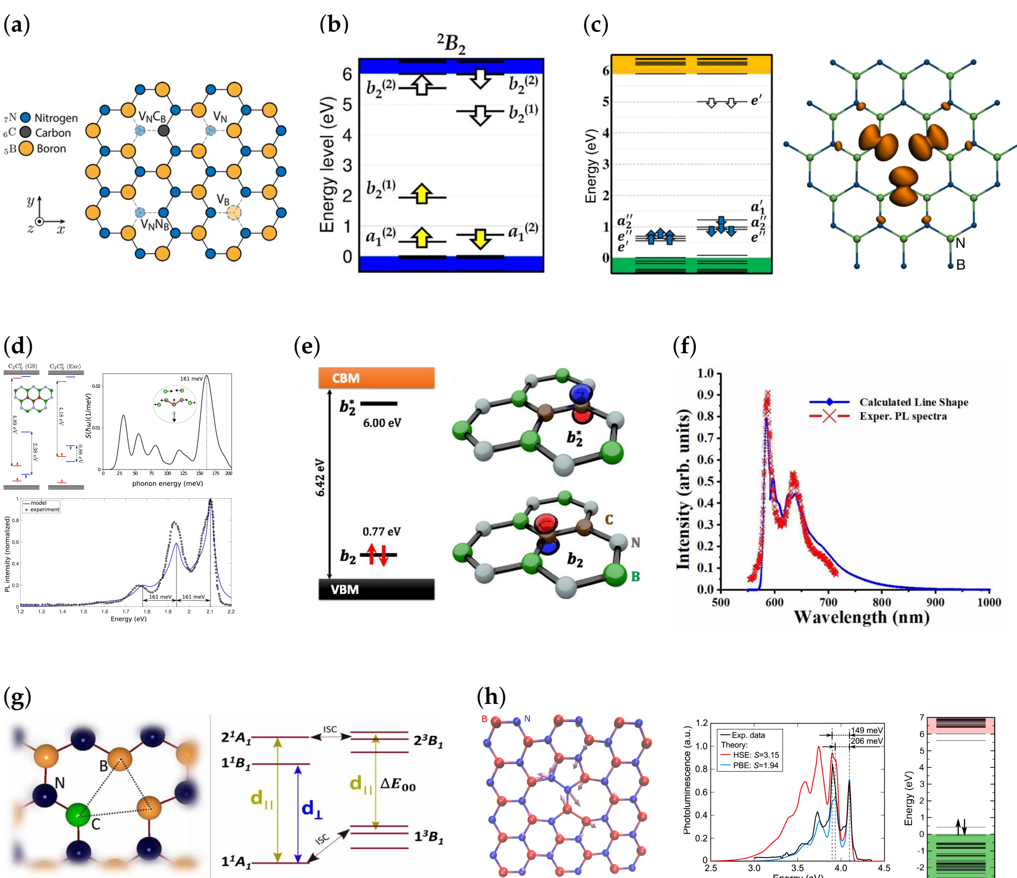

Figure 8. (**a**) Schematic of structures of a selection of defects in hBN. (**b**) Band structure of the N_BV_N defect. (**c**) (**Left**) Band structure of V_B^- and (**Right**) geometry with spin polarised DFT calculation of spin density. (**d**) (**Top left**) Band structure and geometry, (**Top right**) spectral function (inset shows the phonon mode at ∼160 meV) and (**Bottom**) calculated PL spectrum superimposed on the experiment spectrum from ref. [64] of C_2C_N. The ZPL has been shifted by 0.5 eV to align with the experimental spectrum. (**e**) Band structure and wavefunctions of C_BC_N defect. (**f**) Simulated PL spectra of C_BV_N compared to the experimental spectrum from ref. [137]. (**g**) geometry and allowed transitions of C_BV_N with a triplet ground state [147]. (**h**) Geometry, simulated spectra (both Perdew, Burke, and Ernzerhof (PBE) and Heyd, Scuseria, and Ernzerhof (HSE) calculations) and band structure of Stone-Wales defect. Figure 8a,b reprinted with permission from [145]. Copyright 2018 American Chemical Society. Figure 8c adapted from [164] and used under a Creative Commons Attribution 4.0 International (https://creativecommons.org/licenses/by/4.0/, accessed on 9 July 2024) license. Figure 8d adapted with permission from [158]. Copyright 2021 American Chemical Society. Figure 8e reprinted from [155], with the permission of AIP Publishing. Figure 8f,g used with permission of IOP Publishing Ltd, from [147]; permission conveyed through Copyright Clearance Center, Inc. Figure 8h adapted from [142] and used under a Creative Commons Attribution 4.0 International (https://creativecommons.org/licenses/by/4.0/, accessed on 9 July 2024) license.

3. Graphene/hBN Heterostructure Devices for Electrical Control of hBN SPEs

3.1. Stark Tuning of hBN SPEs

As the understanding of hBN based defects developed, fabrication of hBN based devices to further control SPE properties gained significant interest. A popular way of establishing electrical control over hBN SPEs is to assemble graphene (Gr)/hBN heterostructure devices. Monolayer graphene has a similar honeycomb crystal structure and lattice parameter to hBN (a mismatch of 2%), which makes them commensurate materials, and naturally suitable to form a heterostructure when the SPE's geometrical properties need to be protected from strain. Furthermore, the two-dimensional nature of monolayer graphene lends to its large transparency, making it a suitable top layer when coupling SPEs to detectors.

A common way to tune emission lines is to apply an electric field across a SPE to induce a Stark shift in its ZPL emission energy. An early study on the Stark shift of emitters in hBN was performed by forming a Gr/hBN/Gr heterostructure (with multilayer hBN exfoliated from flakes) and using graphene as a top and bottom electrode (Figure 9b) [144]. Due to the low electric field that was able to be applied, there was not a significant shift in the ZPL emission energy. An efficient Stark effect tuning requires a ZPL shift greater than the linewidth, and in such a structure it was not possible to effect such a shift at room temperature. However, a tuning was more obvious when the measurements were performed at 10 K as the thermal broadening of the linewidth was reduced. A key reason behind the limitation over the applied voltages has been the low out-of-plane dielectric constant of hBN, which results in shorting of the device at very low voltages. From Figure 9c, we can see that in this investigation, linear, quadratic and V-shaped Stark shifts were observed. The occurence of the linear Stark shift supports the existence of defects with an out-of-plane dipole. Hence, defects of the form V_NX_B which have a ground state with C_{1h} symmetry cannot be ruled out. Colour centres manifesting quadratic Stark shifts are likely to have a degenerate excited state. In addition to this, it was found that SPEs showing quadratic Stark shifts also had large misalignment between the excitation and emission dipoles, possibly due to them possessing multiple excitation pathways for the relevant electronic transitions. The permanent dipole of the defects exhibiting linear Stark shift were calculated and existed in the range form -0.9 D to 0.9 D and those exhibiting quadratic Stark shifts had a polarisability of $\sim$150 Å^3. For defects with C_{1h} symmetry due to an out-of-plane displacement of the antisite or impurity atom, it is possible to possess a double well potential as the displacement could occur on either side of the host hBN plane. A strong enough electric field and a small energy barrier between the two sites could allow the defect to transition between the two sites and change the sign of the dipole.

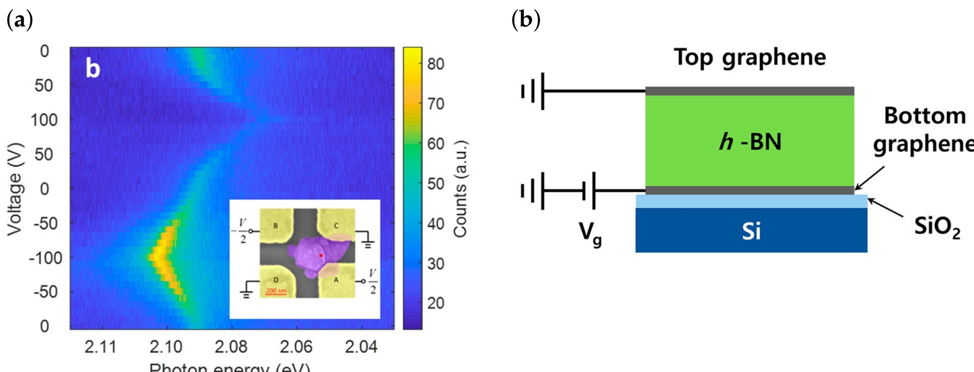

Figure 9. *Cont.*

(**c**)

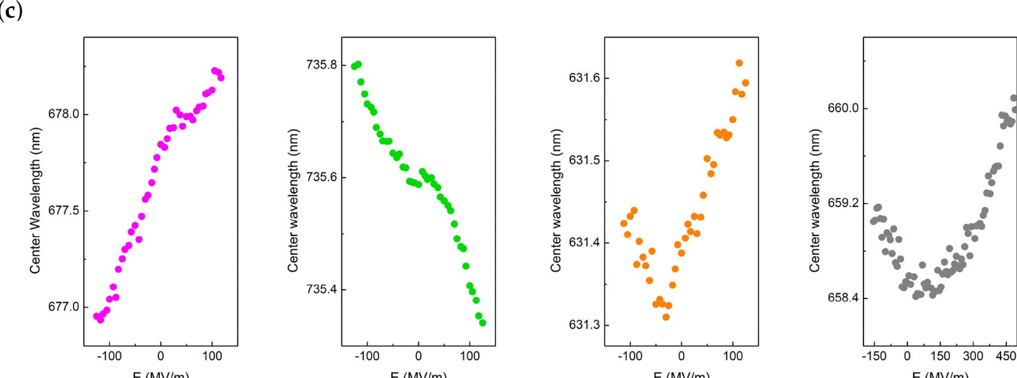

Figure 9. (**a**) Giant Stark shift by using an in-plane nanoscale four-electrode device (device structure shown in inset). (**b**) Gr/hBN/Gr stack used to apply vertical electric fields across defects embedded in hBN. (**c**) Various types of Stark shifts observed using the device stack in (**b**), corresponding to the existence of defects with vastly different dipole orientations. Figure 9a reprinted with permission from [165]. Copyright 2019 American Chemical Society. Figure 9b,c adapted with permission from [144]. Copyright 2018 American Chemical Society.

A mode of inducing larger shifts is to be able to apply larger electric fields without causing breakdown of the device. An example of this was done in an experiment where hBN was deposited on 285 nm of SiO2 (a high *k* dielectric) on Si, followed by a Gr top gate on the hBN [166]. The silicon chip was then back-gated allowing larger fields to be applied. In this study, Stark shifts as large as 24 meV per V/nm was observed at 15 K, which is currently the largest reported Stark shift due to an electric field perpendicular to the plane of the host hBN. Vertical electrical fields can also override charge fluctuations at the hBN/SiO_2 interface and lead to lifetime limited ZPLs at 6.5 K [167].

The two-dimensional nature of hBN leads to defects having an in-plane dipole significantly stronger than a dipole normal to the plane. This motivates the application of an in-plane electric field to effect giant Stark shifts. In a lateral device, a 100 nm thick hBN flake was exfoliated onto two gold electrodes such that an electric field between the electrodes would result in an in-plane electric field [168]. In this device, the Stark shift of blue emitters (transition eneryg of 4.1 eV) was studied and it was found that the Stark shift due to an electric field along the plane was 200 times larger than the shift due to a vertical electric field. DFT calculations of the intrinsic dipole suggests that the defect responsible could be a split interstitial rather than the popular candidate, C_BC_N. Other studies report giant room-temperature Stark shifts of up to 43 meV/(V/nm) by using a nanoscale four-electrode device to perform angle-resolved Stark shifts, shown in Figure 9a, [165]. This allowed shifts 4 times larger than the linewidth of the emitter and, unlike the previous study, was performed on visible light emitters.

3.2. Electrical Charge Control of hBN SPEs

A key step in the scaling up of hBN based photonic quantum technologies is in the fabrication of electrically driven single-photon emitters. Such devices would require on demand charge control of the defects. Recently, it was found that when hBN was deposited on graphene, the majority of SPEs were quenched, possibility due to a combination of charge and energy transfer [169]. It was especially interesting to note that it was only emitters that possessed ZPLs above 600 nm that were quenched. In a recent DFT study of a hBN/Gr bilayer, with the hBN layer hosting native defects, charge transfer was observed between certain defects and absent among others. A deeper investigation of the charge transition levels (CTLs) of the defects, which are the values of the electron chemical potential, μ_e at which there is an equal probability of two charge states of the defect existing (the formation energy of both charge states of the defect is the same at this μ_e), indicated that their location with respect to the Dirac point of graphene determined whether or not charge transfer was thermodynamically favoured (Figure 10a). If the donor (acceptor)

level was above (below) the Dirac point, charge transfer favoured a whole electron was donated (accepted) to (from) Gr [170]. This supported the observation that quenching of emission could be controlled by changing the Fermi level of Gr by functionalising Gr with NMP [169]. However, this does not rule out the role of energy transfer in quenching.

Therefore, interfacing hBN with graphene is a possible scheme to exploit charge control of emitters. This was shown to be possible when studies showed that changing the Fermi level of the graphene layer adjacent to hBN can lead to charging and discharging of the defect (Figure 10c) leading to the defect turning on/off [171,172]. Although the defects in the latter studies were optically excited and not electrically pumped, these studies represented important first steps towards achieving electrical pumping of hBN SPEs. Quenching of emitters due to graphene was also used to spatially localise emitters in hBN [57]. A host hBN layer with emitters activated by Ar annealing was embedded in a trilayer hBN structure, with the encapsulating hBN layer, which was oxygen treated to remove emitters, serving the role of protecting the host layer from the environment. The trilayer stack was then placed on top of a Gr layer with windows patterned using electron beam lithography (Figure 10b). Quenching occured only in areas surrounding the windows where the Gr was in contact with hBN, with emitters directly above the window remaining active. By activating only the emitters in a host layer in the stack, vertical localisation was acheived, and using graphene windows allowed for lateral localisation.

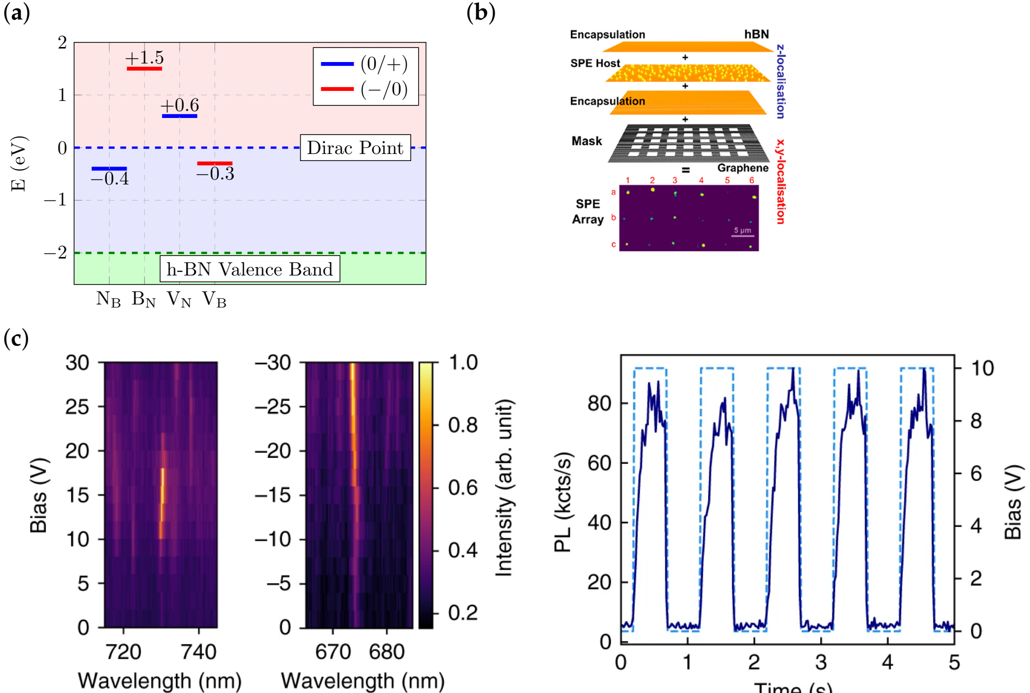

Figure 10. (**a**) Charge transition levels (CTLs) of native defects in hBN with the Dirac point in Gr as a reference. The position of the donor/acceptor relative to the Dirac point determines the directionality and possibility of charge transfer. (**b**) Using a Gr mask and trilayer stack of hBN (with layer hosting emitters embedded in the middle), lateral and vertical localisation of emitters can be achieved by exploiting quenching due to graphene. (**c**) Charge transfer between defects in hBN and graphene can be controlled by manipulating the Fermi level of graphene. This can then be used to turn emitters on/off. Figure 10a adapted from [170] and used under a Creative Commons Attribution 4.0 International license (https://creativecommons.org/licenses/by/4.0/, accessed on 9 July 2024). Figure 10b reprinted with permission from [57]. Copyright 2021 American Chemical Society. Figure 10c adapted from [172] and used under a Creative Commons Attribution 4.0 International license (https://creativecommons.org/licenses/by/4.0/, accessed on 9 July 2024).

4. Challenges and Future Perspectives

In the rapidly evolving field of photonic quantum technologies, hBN has emerged as a material of significant interest. The discovery of room temperature single-photon emitters in a 2D material has opened several prospects in the realisation of large scale quantum photonic technologies. In addition to the topics discussed in the review, significant work is being done in coupling of hBN based emitters to integrated photonic circuits. Integration of single photon emitters (SPEs) with photonic circuits is crucial, as it enables scalable components packaged on a single chip. Generation and coupling of emitters on chip is imperative to package the SPEs with other components that will allow manipulation of light for quantum technology. Early work in this field has focused on flakes of hBN being deposited on silicon nitride (SiN) [173] or aluminium nitride (AlN) waveguides [174]. AlN and SiN are advantageous over Si due to their wide band gap, allowing the full range of emitters to couple into the waveguide without suffering from significant absorption. While successful in demonstrating coupling to waveguides, the efficiency was very low, at about 12% [173]. Monolithic integration of quantum emitters in hBN to waveguides has been demonstrated [175,176]. The advantage of monolithic integration is that it avoids issues of index mismatch present in hybrid integration. In doing so, waveguide coupling and grating coupler efficiencies of $\sim$40% was achieved [175]. Furthermore, by using electron beam irradiation, localisation of emitters to the waveguide could be realised [176]. However, significant work is yet to do be done for high throughput fabrication of such devices. Firstly, the process of using hBN flakes makes deterministic aligning of emitter dipoles to the waveguide challenging and secondly, the dimensions of the flakes prevents wafer scale fabrication of these devices. It is therefore of interest to design a protocol which allows control over dipole alignment, emitter placement and wafer scale processing. For example, the CVD process for hBN on (SiN) substrates represents a promising advancement.

Enhancement of SPE intensities to achieve high bit rates across communications platforms is also an area that needs to be advanced. This can be achieved by coupling emitters to resonant cavities [177,178]. Present challenges to this is similar to the coupling of waveguides to emitters, i.e alignment of dipoles to the cavity to achieve maximal Purcell enhancement. Current work has only been able to achieve moderate enhancement on emitters in hBN flakes of 2 to 6 times [177,178].

The introduction of dopants into hBN to create resonant peaks suitable for single-photon sources is an innovative approach that warrants further exploration. Precise engineering of defects with desirable optical and spin properties will allow major leaps in quantum computation and communications relying on optically addressable spin qubits. The search for suitable defects and methods for their creation can be guided by theoretical modelling. Current limitations to first-principles modelling of defects include high computational cost of state-of-the-art exchange-correlation functionals, such as HSE, and calculations of dynamical properties, such as spectra, often done using the GW (G-for the one-particle Green's function and W- for the screened Coloumb interaction)-BSE (Bethe-Salpeter Equation) approximation, generating function approaches or polaron models. It is therefore useful to know the performance of static DFT using standard commonly available exchange-correlation functionals such as PBE and LDA (local density approximation) in deriving different properties of systems when compared to state-of-the-art methods, as these have a lower computational cost [179]. If some properties, such as the dielectric function and density of states (DOS) of hBN hosting colour centres can be obtained using standard DFT parameters, then a larger scope of defects can be screened to discover ideal candidate defects as SPEs.

Finally, in order to fully realise a compact quantum technology that can be integrated with other electrical or photonic components. It becomes necessary to be able to electrically drive emission. While some work has be done on emitters in InGaN/GaN QDs [180], and TMDs [181], these sources are not as feasible for scaling due to their bulk (GaN) or low temperature (TMDs) nature. Therefore, further study needs to be performed on controlled carrier injection into defects in hBN to achieve electroluminescence.

In conclusion, the future of photonic quantum technologies based on hBN holds immense promise. The continued refinement of fabrication processes, such as the CVD process for hBN on SiN substrates, will be instrumental in harnessing the full potential of this field. As our understanding of quantum phenomena deepens and our ability to manipulate quantum systems improves, we anticipate a wealth of exciting breakthroughs in the coming years for hBN based photonic quantum technologies.

Author Contributions: Conceptualization, M.K.P., C.-C.H., J.D.M. and Y.-L.D.H.; methodology, M.K.P., C.-C.H., J.D.M. and Y.-L.D.H.; investigation, M.K.P. and M.P.C.T.; writing—original draft preparation, M.K.P.; writing—review and editing, M.K.P., M.P.C.T., C.-C.H., J.D.M. and Y.-L.D.H; supervision, C.-C.H., J.D.M. and Y.-L.D.H. All authors have read and agreed to the published version of the manuscript.

Funding: The work was supported by the Engineering and Physical Sciences Research Council (EPSRC), grant number EP/N00762X/1, EP/V040030/1 and EP/Y003551/1.

Informed Consent Statement: Not applicable.

Data Availability Statement: The raw data supporting the conclusions of this article will be made available by the authors on request.

Conflicts of Interest: The authors declare no conflict of interest.

References

1. Tran, T.T.; Bray, K.; Ford, M.J.; Toth, M.; Aharonovich, I. Quantum emission from hexagonal boron nitride monolayers. *Nat. Nanotechnol.* **2016**, *11*, 37–41. [CrossRef]
2. Wang, J.; Ma, F.; Sun, M. Graphene, hexagonal boron nitride, and their heterostructures: properties and applications. *RSC Adv.* **2017**, *7*, 16801–16822. [CrossRef]
3. Bhimanapati, G.R.; Glavin, N.R.; Robinson, J.A., Chapter Three—2D Boron Nitride: Synthesis and Applications. In *2D Materials*; Elsevier: Amsterdam, The Netherlands, 2016; Volume 95, pp. 101–147. [CrossRef]
4. Kimura, Y.; Wakabayashi, T.; Okada, K.; Wada, T.; Nishikawa, H. Boron nitride as a lubricant additive. *Wear* **1999**, *232*, 199–206. [CrossRef]
5. Constantinescu, G.; Kuc, A.; Heine, T. Stacking in bulk and bilayer hexagonal boron nitride. *Phys. Rev. Lett.* **2013**, *111*, 036104. [CrossRef] [PubMed]
6. Chen, L.; Elibol, K.; Cai, H.; Jiang, C.; Shi, W.; Chen, C.; Wang, H.S.; Wang, X.; Mu, X.; Li, C.; et al. Direct observation of layer-stacking and oriented wrinkles in multilayer hexagonal boron nitride. *2D Mater.* **2021**, *8*, 024001. [CrossRef]
7. Ji, Y.; Calderon, B.; Han, Y.; Cueva, P.; Jungwirth, N.R.; Alsalman, H.A.; Hwang, J.; Fuchs, G.D.; Muller, D.A.; Spencer, M.G. Chemical vapor deposition growth of large single-crystal mono-, bi-, tri-layer hexagonal boron nitride and their interlayer stacking. *ACS Nano* **2017**, *11*, 12057–12066. [CrossRef] [PubMed]
8. Alem, N.; Erni, R.; Kisielowski, C.; Rossell, M.D.; Gannett, W.; Zettl, A. Atomically thin hexagonal boron nitride probed by ultrahigh-resolution transmission electron microscopy. *Phys. Rev. B* **2009**, *80*, 155425. [CrossRef]
9. Gorbachev, R.V.; Riaz, I.; Nair, R.R.; Jalil, R.; Britnell, L.; Belle, B.D.; Hill, E.W.; Novoselov, K.S.; Watanabe, K.; Taniguchi, T.; et al. Hunting for Monolayer Boron Nitride: Optical and Raman Signatures. *Small* **2011**, *7*, 465–468. [CrossRef]
10. Nagashima, A.; Tejima, N.; Gamou, Y.; Kawai, T.; Oshima, C. Electronic states of monolayer hexagonal boron nitride formed on the metal surfaces. *Surf. Sci.* **1996**, *357*, 307–311. [CrossRef]
11. Ooi, N.; Rairkar, A.; Lindsley, L.; Adams, J. Electronic structure and bonding in hexagonal boron nitride. *J. Phys. Condens. Matter* **2005**, *18*, 97. [CrossRef]
12. Blase, X.; Rubio, A.; Louie, S.G.; Cohen, M.L. Quasiparticle band structure of bulk hexagonal boron nitride and related systems. *Phys. Rev. B* **1995**, *51*, 6868. [CrossRef]
13. Xu, Y.N.; Ching, W. Calculation of ground-state and optical properties of boron nitrides in the hexagonal, cubic, and wurtzite structures. *Phys. Rev. B* **1991**, *44*, 7787. [CrossRef]
14. Gao, S.P. Crystal structures and band gap characters of h-BN polytypes predicted by the dispersion corrected DFT and GW method. *Solid State Commun.* **2012**, *152*, 1817–1820. [CrossRef]
15. Topsakal, M.; Aktürk, E.; Ciraci, S. First-principles study of two- and one-dimensional honeycomb structures of boron nitride. *Phys. Rev. B Condens. Matter Mater. Phys.* **2009**, *79*, 115442. [CrossRef]
16. Paleari, F.; Galvani, T.; Amara, H.; Ducastelle, F.; Molina-Sánchez, A.; Wirtz, L. Excitons in few-layer hexagonal boron nitride: Davydov splitting and surface localization. *2D Mater.* **2018**, *5*, 045017. [CrossRef]
17. Zunger, A.; Katzir, A.; Halperin, A. Optical properties of hexagonal boron nitride. *Phys. Rev. B* **1976**, *13*, 5560. [CrossRef]

18. Evans, D.; McGlynn, A.G.; Towlson, B.M.; Gunn, M.; Jones, D.; Jenkins, T.E.; Winter, R.; Poolton, N.R. Determination of the optical band-gap energy of cubic and hexagonal boron nitride using luminescence excitation spectroscopy. *J. Phys. Condens. Matter* **2008**, *20*, 075233. [CrossRef]
19. Watanabe, K.; Taniguchi, T.; Kanda, H. Direct-bandgap properties and evidence for ultraviolet lasing of hexagonal boron nitride single crystal. *Nat. Mater.* **2004**, *3*, 404–409. [CrossRef]
20. Elias, C.; Valvin, P.; Pelini, T.; Summerfield, A.; Mellor, C.J.; Cheng, T.S.; Eaves, L.; Foxon, C.T.; Beton, P.H.; Novikov, S.V.; et al. Direct band-gap crossover in epitaxial monolayer boron nitride. *Nat. Commun.* **2019**, *10*, 2639. [CrossRef] [PubMed]
21. Wickramaratne, D.; Weston, L.; Walle, C.G.V.D. Monolayer to Bulk Properties of Hexagonal Boron Nitride. *J. Phys. Chem. C* **2018**, *122*, 25524–25529. [CrossRef]
22. Cassabois, G.; Valvin, P.; Gil, B. Hexagonal boron nitride is an indirect bandgap semiconductor. *Nat. Photonics* **2016**, *10*, 262–266. [CrossRef]
23. Schuster, R.; Habenicht, C.; Ahmad, M.; Knupfer, M.; Büchner, B. Direct observation of the lowest indirect exciton state in the bulk of hexagonal boron nitride. *Phys. Rev. B* **2018**, *97*, 041201. [CrossRef]
24. Mak, K.F.; Lee, C.; Hone, J.; Shan, J.; Heinz, T.F. Atomically thin MoS_2: A new direct-gap semiconductor. *Phys. Rev. Lett.* **2010**, *105*, 136805. [CrossRef] [PubMed]
25. Henck, H.; Pierucci, D.; Fugallo, G.; Avila, J.; Cassabois, G.; Dappe, Y.J.; Silly, M.G.; Chen, C.; Gil, B.; Gatti, M.; et al. Direct observation of the band structure in bulk hexagonal boron nitride. *Phys. Rev. B* **2017**, *95*, 085410. [CrossRef]
26. Nagashima, A.; Tejima, N.; Gamou, Y.; Kawai, T.; Oshima, C. Electronic structure of monolayer hexagonal boron nitride physisorbed on metal surfaces. *Phys. Rev. Lett.* **1995**, *75*, 3918. [CrossRef]
27. Geick, R.; Perry, C.H.; Rupprecht, G. Normal modes in hexagonal boron nitride. *Phys. Rev.* **1966**, *146*, 543. [CrossRef]
28. Serrano, J.; Bosak, A.; Arenal, R.; Krisch, M.; Watanabe, K.; Taniguchi, T.; Kanda, H.; Rubio, A.; Wirtz, L. Vibrational properties of hexagonal boron nitride: Inelastic X-ray scattering and Ab Initio calculations. *Phys. Rev. Lett.* **2007**, *98*, 095503. [CrossRef]
29. Kim, K.K.; Hsu, A.; Jia, X.; Kim, S.M.; Shi, Y.; Hofmann, M.; Nezich, D.; Rodriguez-Nieva, J.F.; Dresselhaus, M.; Palacios, T.; et al. Synthesis of monolayer hexagonal boron nitride on Cu foil using chemical vapor deposition. *Nano Lett.* **2012**, *12*, 161–166. [CrossRef] [PubMed]
30. Wang, S.; Crowther, J.; Kageshima, H.; Hibino, H.; Taniyasu, Y. Epitaxial intercalation growth of scalable hexagonal boron nitride/graphene bilayer moiré materials with highly convergent interlayer angles. *ACS Nano* **2021**, *15*, 14384–14393. [CrossRef]
31. Shi, Y.; Hamsen, C.; Jia, X.; Kim, K.K.; Reina, A.; Hofmann, M.; Hsu, A.L.; Zhang, K.; Li, H.; Juang, Z.Y.; et al. Synthesis of few-layer hexagonal boron nitride thin film by chemical vapor deposition. *Nano Lett.* **2010**, *10*, 4134–4139. [CrossRef]
32. Taniguchi, T.; Watanabe, K. Synthesis of high-purity boron nitride single crystals under high pressure by using Ba–BN solvent. *J. Cryst. Growth* **2007**, *303*, 525–529. [CrossRef]
33. Kubota, Y.; Watanabe, K.; Tsuda, O.; Taniguchi, T. Deep ultraviolet light-emitting hexagonal boron nitride synthesized at atmospheric pressure. *Science* **2007**, *317*, 932–934. [CrossRef] [PubMed]
34. Wang, Z.; Tang, Z.; Xue, Q.; Huang, Y.; Huang, Y.; Zhu, M.; Pei, Z.; Li, H.; Jiang, H.; Fu, C.; et al. Fabrication of boron nitride nanosheets by exfoliation. *Chem. Rec.* **2016**, *16*, 1204–1215. [CrossRef]
35. Gonzalez Ortiz, D.; Pochat-Bohatier, C.; Cambedouzou, J.; Bechelany, M.; Miele, P. Exfoliation of hexagonal boron nitride (h-BN) in liquid phase by ion intercalation. *Nanomaterials* **2018**, *8*, 716. [CrossRef] [PubMed]
36. Rafiei-Sarmazdeh, Z.; Jafari, S.H.; Ahmadi, S.J.; Zahedi-Dizaji, S.M. Large-scale exfoliation of hexagonal boron nitride with combined fast quenching and liquid exfoliation strategies. *J. Mater. Sci.* **2016**, *51*, 3162–3169. [CrossRef]
37. Khan, U.; May, P.; O'Neill, A.; Bell, A.P.; Boussac, E.; Martin, A.; Semple, J.; Coleman, J.N. Polymer reinforcement using liquid-exfoliated boron nitride nanosheets. *Nanoscale* **2013**, *5*, 581–587. [CrossRef] [PubMed]
38. Lee, K.H.; Shin, H.J.; Lee, J.; Lee, I.y.; Kim, G.H.; Choi, J.Y.; Kim, S.W. Large-scale synthesis of high-quality hexagonal boron nitride nanosheets for large-area graphene electronics. *Nano Lett.* **2012**, *12*, 714–718. [CrossRef]
39. Lee, J.S.; Choi, S.H.; Yun, S.J.; Kim, Y.I.; Boandoh, S.; Park, J.H.; Shin, B.G.; Ko, H.; Lee, S.H.; Kim, Y.M.; et al. Wafer-scale single-crystal hexagonal boron nitride film via self-collimated grain formation. *Science* **2018**, *362*, 817–821. [CrossRef]
40. Lin, W.H.; Brar, V.W.; Jariwala, D.; Sherrott, M.C.; Tseng, W.S.; Wu, C.I.; Yeh, N.C.; Atwater, H.A. Atomic-scale structural and chemical characterization of hexagonal boron nitride layers synthesized at the wafer-scale with monolayer thickness control. *Chem. Mater.* **2017**, *29*, 4700–4707. [CrossRef]
41. Jang, A.R.; Hong, S.; Hyun, C.; Yoon, S.I.; Kim, G.; Jeong, H.Y.; Shin, T.J.; Park, S.O.; Wong, K.; Kwak, S.K.; et al. Wafer-scale and wrinkle-free epitaxial growth of single-orientated multilayer hexagonal boron nitride on sapphire. *Nano Lett.* **2016**, *16*, 3360–3366. [CrossRef]
42. Song, L.; Ci, L.; Lu, H.; Sorokin, P.B.; Jin, C.; Ni, J.; Kvashnin, A.G.; Kvashnin, D.G.; Lou, J.; Yakobson, B.I.; et al. Large scale growth and characterization of atomic hexagonal boron nitride layers. *Nano Lett.* **2010**, *10*, 3209–3215. [CrossRef]
43. Kim, S.M.; Hsu, A.; Park, M.H.; Chae, S.H.; Yun, S.J.; Lee, J.S.; Cho, D.H.; Fang, W.; Lee, C.; Palacios, T.; et al. Synthesis of large-area multilayer hexagonal boron nitride for high material performance. *Nat. Commun.* **2015**, *6*, 8662. [CrossRef]
44. Binder, J.; Dabrowska, A.K.; Tokarczyk, M.; Rousseau, A.; Valvin, P.; Bozek, R.; Nogajewski, K.; Kowalski, G.; Pacuski, W.; Gil, B.; et al. Homoepitaxy of Boron Nitride on Exfoliated Hexagonal Boron Nitride Flakes. *Nano Lett.* **2024**, *24*, 6990–6996. [CrossRef]
45. Wang, L.; Xu, X.; Zhang, L.; Qiao, R.; Wu, M.; Wang, Z.; Zhang, S.; Liang, J.; Zhang, Z.; Zhang, Z.; et al. Epitaxial growth of a 100-square-centimetre single-crystal hexagonal boron nitride monolayer on copper. *Nature* **2019**, *570*, 91–95. [CrossRef]

46. Chen, T.A.; Chuu, C.P.; Tseng, C.C.; Wen, C.K.; Wong, H.S.P.; Pan, S.; Li, R.; Chao, T.A.; Chueh, W.C.; Zhang, Y.; et al. Wafer-scale single-crystal hexagonal boron nitride monolayers on Cu (111). *Nature* **2020**, *579*, 219–223. [CrossRef] [PubMed]
47. Hemmi, A.; Cun, H.; Brems, S.; Huyghebaert, C.; Greber, T. Wafer-scale, epitaxial growth of single layer hexagonal boron nitride on Pt (111). *J. Phys. Mater.* **2021**, *4*, 044012. [CrossRef]
48. Jeong, H.; Kim, D.Y.; Kim, J.; Moon, S.; Han, N.; Lee, S.H.; Okello, O.F.N.; Song, K.; Choi, S.Y.; Kim, J.K. Wafer-scale and selective-area growth of high-quality hexagonal boron nitride on Ni (111) by metal-organic chemical vapor deposition. *Sci. Rep.* **2019**, *9*, 5736. [CrossRef] [PubMed]
49. Dos Santos, R.B.; Rivelino, R.; de Brito Mota, F.; Kakanakova-Georgieva, A.; Gueorguiev, G.K. Feasibility of novel (H 3 C) n X (SiH 3) 3- n compounds (X= B, Al, Ga, In): Structure, stability, reactivity, and Raman characterization from ab initio calculations. *Dalton Trans.* **2015**, *44*, 3356–3366. [CrossRef]
50. Reina, A.; Jia, X.; Ho, J.; Nezich, D.; Son, H.; Bulovic, V.; Dresselhaus, M.S.; Kong, J. Large area, few-layer graphene films on arbitrary substrates by chemical vapor deposition. *Nano Lett.* **2009**, *9*, 30–35. [CrossRef]
51. Fukamachi, S.; Solís-Fernández, P.; Kawahara, K.; Tanaka, D.; Otake, T.; Lin, Y.C.; Suenaga, K.; Ago, H. Large-area synthesis and transfer of multilayer hexagonal boron nitride for enhanced graphene device arrays. *Nat. Electron.* **2023**, *6*, 126–136. [CrossRef]
52. Scheuer, K.; Hornig, G.; DeCorby, R. Polymer transfer technique for strain-activated emission in hexagonal boron nitride. *Opt. Express* **2021**, *29*, 26103–26115. [CrossRef]
53. Wang, R.; Purdie, D.G.; Fan, Y.; Massabuau, F.C.P.; Braeuninger-Weimer, P.; Burton, O.J.; Blume, R.; Schloegl, R.; Lombardo, A.; Weatherup, R.S.; et al. A peeling approach for integrated manufacturing of large monolayer h-BN crystals. *ACS Nano* **2019**, *13*, 2114–2126. [CrossRef] [PubMed]
54. Zhang, G.; Guell, A.G.; Kirkman, P.M.; Lazenby, R.A.; Miller, T.S.; Unwin, P.R. Versatile polymer-free graphene transfer method and applications. *ACS Appl. Mater. Interfaces* **2016**, *8*, 8008–8016. [CrossRef] [PubMed]
55. Li, X.; Sundaram, S.; El Gmili, Y.; Ayari, T.; Puybaret, R.; Patriarche, G.; Voss, P.L.; Salvestrini, J.P.; Ougazzaden, A. Large-area two-dimensional layered hexagonal boron nitride grown on sapphire by metalorganic vapor phase epitaxy. *Cryst. Growth Des.* **2016**, *16*, 3409–3415. [CrossRef]
56. Garcia, A.G.; Neumann, M.; Amet, F.; Williams, J.R.; Watanabe, K.; Taniguchi, T.; Goldhaber-Gordon, D. Effective cleaning of hexagonal boron nitride for graphene devices. *Nano Lett.* **2012**, *12*, 4449–4454. [CrossRef]
57. Stewart, J.C.; Fan, Y.; Danial, J.S.; Goetz, A.; Prasad, A.S.; Burton, O.J.; Alexander-Webber, J.A.; Lee, S.F.; Skoff, S.M.; Babenko, V.; et al. Quantum Emitter Localization in Layer-Engineered Hexagonal Boron Nitride. *ACS Nano* **2021**, *15*, 13591–13603. [CrossRef] [PubMed]
58. Song, Y.; Zhang, C.; Li, B.; Ding, G.; Jiang, D.; Wang, H.; Xie, X. Van der Waals epitaxy and characterization of hexagonal boron nitride nanosheets on graphene. *Nanoscale Res. Lett.* **2014**, *9*, 367. [CrossRef]
59. Liu, Z.; Song, L.; Zhao, S.; Huang, J.; Ma, L.; Zhang, J.; Lou, J.; Ajayan, P.M. Direct growth of graphene/hexagonal boron nitride stacked layers. *Nano Lett.* **2011**, *11*, 2032–2037. [CrossRef]
60. Zhu, Z.; Zhang, Z.; Wang, S.; Zou, J.; Gan, Y.; Yang, R.; Zhang, Y.; Long, B. Hexagonal Boron Nitride Thick Film Grown on a Sapphire Substrate via Low-Pressure Chemical Vapor Deposition. *Cryst. Growth Des.* **2023**, *23*, 7662–7668. [CrossRef]
61. Chugh, D.; Wong-Leung, J.; Li, L.; Lysevych, M.; Tan, H.H.; Jagadish, C. Flow modulation epitaxy of hexagonal boron nitride. *2D Mater.* **2018**, *5*, 045018. [CrossRef]
62. Musiał, A.; Holewa, P.; Wyborski, P.; Syperek, M.; Kors, A.; Reithmaier, J.P.; Sęk, G.; Benyoucef, M. High-purity triggered single-photon emission from symmetric single InAs/InP quantum dots around the telecom C-band window. *Adv. Quantum Technol.* **2020**, *3*, 1900082. [CrossRef]
63. Koperski, M.; Nogajewski, K.; Arora, A.; Cherkez, V.; Mallet, P.; Veuillen, J.Y.; Marcus, J.; Kossacki, P.; Potemski, M. Single photon emitters in exfoliated WSe2 structures. *Nat. Nanotechnol.* **2015**, *10*, 503–506. [CrossRef]
64. Martínez, L.; Pelini, T.; Waselowski, V.; Maze, J.; Gil, B.; Cassabois, G.; Jacques, V. Efficient single photon emission from a high-purity hexagonal boron nitride crystal. *Phys. Rev. B* **2016**, *94*, 121405. [CrossRef]
65. Grosso, G.; Moon, H.; Lienhard, B.; Ali, S.; Efetov, D.K.; Furchi, M.M.; Jarillo-Herrero, P.; Ford, M.J.; Aharonovich, I.; Englund, D. Tunable and high-purity room temperature single-photon emission from atomic defects in hexagonal boron nitride. *Nat. Commun.* **2017**, *8*, 705. [CrossRef]
66. Bourrellier, R.; Meuret, S.; Tararan, A.; Stéphan, O.; Kociak, M.; Tizei, L.H.; Zobelli, A. Bright UV single photon emission at point defects in h-BN. *Nano Lett.* **2016**, *16*, 4317–4321. [CrossRef]
67. Tran, T.T.; Elbadawi, C.; Totonjian, D.; Lobo, C.J.; Grosso, G.; Moon, H.; Englund, D.R.; Ford, M.J.; Aharonovich, I.; Toth, M. Robust multicolor single photon emission from point defects in hexagonal boron nitride. *ACS Nano* **2016**, *10*, 7331–7338. [CrossRef]
68. Xu, Z.Q.; Elbadawi, C.; Tran, T.T.; Kianinia, M.; Li, X.; Liu, D.; Hoffman, T.B.; Nguyen, M.; Kim, S.; Edgar, J.H.; et al. Single photon emission from plasma treated 2D hexagonal boron nitride. *Nanoscale* **2018**, *10*, 7957–7965. [CrossRef]
69. Miyazawa, T.; Takemoto, K.; Nambu, Y.; Miki, S.; Yamashita, T.; Terai, H.; Fujiwara, M.; Sasaki, M.; Sakuma, Y.; Takatsu, M.; et al. Single-photon emission at 1.5 µm from an InAs/InP quantum dot with highly suppressed multi-photon emission probabilities. *Appl. Phys. Lett.* **2016**, *109*, 132106. [CrossRef]
70. Zhao, H.; Pettes, M.T.; Zheng, Y.; Htoon, H. Site-controlled telecom-wavelength single-photon emitters in atomically-thin $MoTe_2$. *Nat. Commun.* **2021**, *12*, 6753. [CrossRef]

71. Schröder, T.; Gädeke, F.; Banholzer, M.J.; Benson, O. Ultrabright and efficient single-photon generation based on nitrogen-vacancy centres in nanodiamonds on a solid immersion lens. *New J. Phys.* **2011**, *13*, 055017. [CrossRef]
72. Zhao, H.Q.; Fujiwara, M.; Takeuchi, S. Suppression of fluorescence phonon sideband from nitrogen vacancy centers in diamond nanocrystals by substrate effect. *Opt. Express* **2012**, *20*, 15628–15635. [CrossRef] [PubMed]
73. Pezzagna, S.; Rogalla, D.; Wildanger, D.; Meijer, J.; Zaitsev, A. Creation and nature of optical centres in diamond for single-photon emission—overview and critical remarks. *New J. Phys.* **2011**, *13*, 035024. [CrossRef]
74. Jelezko, F.; Tietz, C.; Gruber, A.; Popa, I.; Nizovtsev, A.; Kilin, S.; Wrachtrup, J. Spectroscopy of Single N-V Centers in Diamond. *Single Mol.* **2001**, *2*, 255–260. [CrossRef]
75. Jelezko, F.; Wrachtrup, J. Single defect centres in diamond: A review. *Phys. Status Solidi (a)* **2006**, *203*, 3207–3225. [CrossRef]
76. Neu, E.; Steinmetz, D.; Riedrich-Möller, J.; Gsell, S.; Fischer, M.; Schreck, M.; Becher, C. Single photon emission from silicon-vacancy colour centres in chemical vapour deposition nano-diamonds on iridium. *New J. Phys.* **2011**, *13*, 025012. [CrossRef]
77. Neu, E.; Hepp, C.; Hauschild, M.; Gsell, S.; Fischer, M.; Sternschulte, H.; Steinmüller-Nethl, D.; Schreck, M.; Becher, C. Low-temperature investigations of single silicon vacancy colour centres in diamond. *New J. Phys.* **2013**, *15*, 043005. [CrossRef]
78. Lindner, S.; Bommer, A.; Muzha, A.; Krueger, A.; Gines, L.; Mandal, S.; Williams, O.; Londero, E.; Gali, A.; Becher, C. Strongly inhomogeneous distribution of spectral properties of silicon-vacancy color centers in nanodiamonds. *New J. Phys.* **2018**, *20*, 115002. [CrossRef]
79. Dusanowski, Ł.; Syperek, M.; Misiewicz, J.; Somers, A.; Hoefling, S.; Kamp, M.; Reithmaier, J.; Sęk, G. Single-photon emission of InAs/InP quantum dashes at 1.55 µm and temperatures up to 80 K. *Appl. Phys. Lett.* **2016**, *108*, 163108. [CrossRef]
80. Sapienza, L.; Davanço, M.; Badolato, A.; Srinivasan, K. Nanoscale optical positioning of single quantum dots for bright and pure single-photon emission. *Nat. Commun.* **2015**, *6*, 7833. [CrossRef]
81. Chen, Z.S.; Ma, B.; Shang, X.J.; Ni, H.Q.; Wang, J.L.; Niu, Z.C. Bright single-photon source at 1.3 µm based on InAs bilayer quantum dot in micropillar. *Nanoscale Res. Lett.* **2017**, *12*, 378. [CrossRef]
82. Castelletto, S.; Johnson, B.; Ivády, V.; Stavrias, N.; Umeda, T.; Gali, A.; Ohshima, T. A silicon carbide room-temperature single-photon source. *Nat. Mater.* **2014**, *13*, 151–156. [CrossRef] [PubMed]
83. Wang, J.; Zhou, Y.; Wang, Z.; Rasmita, A.; Yang, J.; Li, X.; von Bardeleben, H.J.; Gao, W. Bright room temperature single photon source at telecom range in cubic silicon carbide. *Nat. Commun.* **2018**, *9*, 4106. [CrossRef] [PubMed]
84. Nagy, R.; Widmann, M.; Niethammer, M.; Dasari, D.B.; Gerhardt, I.; Soykal, Ö.O.; Radulaski, M.; Ohshima, T.; Vučković, J.; Son, N.T.; et al. Quantum properties of dichroic silicon vacancies in silicon carbide. *Phys. Rev. Appl.* **2018**, *9*, 034022. [CrossRef]
85. Udvarhelyi, P.; Thiering, G.; Morioka, N.; Babin, C.; Kaiser, F.; Lukin, D.; Ohshima, T.; Ul-Hassan, J.; Son, N.T.; Vučković, J.; et al. Vibronic states and their effect on the temperature and strain dependence of silicon-vacancy qubits in 4 h-si c. *Phys. Rev. Appl.* **2020**, *13*, 054017. [CrossRef]
86. Lohrmann, A.; Iwamoto, N.; Bodrog, Z.; Castelletto, S.; Ohshima, T.; Karle, T.; Gali, A.; Prawer, S.; McCallum, J.; Johnson, B. Single-photon emitting diode in silicon carbide. *Nat. Commun.* **2015**, *6*, 7783. [CrossRef]
87. Ivády, V.; Davidsson, J.; Son, N.T.; Ohshima, T.; Abrikosov, I.A.; Gali, A. Identification of Si-vacancy related room-temperature qubits in 4 H silicon carbide. *Phys. Rev. B* **2017**, *96*, 161114. [CrossRef]
88. Koehl, W.F.; Buckley, B.B.; Heremans, F.J.; Calusine, G.; Awschalom, D.D. Room temperature coherent control of defect spin qubits in silicon carbide. *Nature* **2011**, *479*, 84–87. [CrossRef] [PubMed]
89. Babunts, R.; Vetrov, V.; Il'in, I.; Mokhov, E.; Romanov, N.; Khramtsov, V.; Baranov, P. Properties of erbium luminescence in bulk crystals of silicon carbide. *Phys. Solid State* **2000**, *42*, 829–835. [CrossRef]
90. He, Y.M.; Clark, G.; Schaibley, J.R.; He, Y.; Chen, M.C.; Wei, Y.J.; Ding, X.; Zhang, Q.; Yao, W.; Xu, X.; et al. Single quantum emitters in monolayer semiconductors. *Nat. Nanotechnol.* **2015**, *10*, 497–502. [CrossRef]
91. Lee, Y.; Hu, Y.; Lang, X.; Kim, D.; Li, K.; Ping, Y.; Fu, K.M.C.; Cho, K. Spin-defect qubits in two-dimensional transition metal dichalcogenides operating at telecom wavelengths. *Nat. Commun.* **2022**, *13*, 7501. [CrossRef]
92. He, X.; Hartmann, N.F.; Ma, X.; Kim, Y.; Ihly, R.; Blackburn, J.L.; Gao, W.; Kono, J.; Yomogida, Y.; Hirano, A.; et al. Tunable room-temperature single-photon emission at telecom wavelengths from sp 3 defects in carbon nanotubes. *Nat. Photonics* **2017**, *11*, 577–582. [CrossRef]
93. Endo, T.; Ishi-Hayase, J.; Maki, H. Photon antibunching in single-walled carbon nanotubes at telecommunication wavelengths and room temperature. *Appl. Phys. Lett.* **2015**, *106*, 113106 . [CrossRef]
94. Ma, X.; Hartmann, N.F.; Baldwin, J.K.; Doorn, S.K.; Htoon, H. Room-temperature single-photon generation from solitary dopants of carbon nanotubes. *Nat. Nanotechnol.* **2015**, *10*, 671–675. [CrossRef]
95. Ghosh, S.; Bachilo, S.M.; Simonette, R.A.; Beckingham, K.M.; Weisman, R.B. Oxygen doping modifies near-infrared band gaps in fluorescent single-walled carbon nanotubes. *Science* **2010**, *330*, 1656–1659. [CrossRef]
96. Piao, Y.; Meany, B.; Powell, L.R.; Valley, N.; Kwon, H.; Schatz, G.C.; Wang, Y. Brightening of carbon nanotube photoluminescence through the incorporation of sp 3 defects. *Nat. Chem.* **2013**, *5*, 840–845. [CrossRef]
97. Miyauchi, Y.; Iwamura, M.; Mouri, S.; Kawazoe, T.; Ohtsu, M.; Matsuda, K. Brightening of excitons in carbon nanotubes on dimensionality modification. *Nat. Photonics* **2013**, *7*, 715–719. [CrossRef]
98. Tamariz, S.; Callsen, G.; Stachurski, J.; Shojiki, K.; Butté, R.; Grandjean, N. Toward bright and pure single photon emitters at 300 K based on GaN quantum dots on silicon. *ACS Photonics* **2020**, *7*, 1515–1522. [CrossRef]

99. Kako, S.; Santori, C.; Hoshino, K.; Götzinger, S.; Yamamoto, Y.; Arakawa, Y. A gallium nitride single-photon source operating at 200 K. *Nat. Mater.* **2006**, *5*, 887–892. [CrossRef]
100. Arita, M.; Le Roux, F.; Holmes, M.J.; Kako, S.; Arakawa, Y. Ultraclean single photon emission from a GaN quantum dot. *Nano Lett.* **2017**, *17*, 2902–2907. [CrossRef]
101. Meunier, M.; Eng, J.J.; Mu, Z.; Chenot, S.; Brändli, V.; de Mierry, P.; Gao, W.; Zúñiga-Pérez, J. Telecom single-photon emitters in GaN operating at room temperature: embedment into bullseye antennas. *Nanophotonics* **2023**, *12*, 1405–1419. [CrossRef]
102. Holmes, M.J.; Choi, K.; Kako, S.; Arita, M.; Arakawa, Y. Room-temperature triggered single photon emission from a III-nitride site-controlled nanowire quantum dot. *Nano Lett.* **2014**, *14*, 982–986. [CrossRef] [PubMed]
103. Ma, L.P.; Ren, W.; Cheng, H.M. Transfer methods of graphene from metal substrates: A review. *Small Methods* **2019**, *3*, 1900049. [CrossRef]
104. Choi, S.; Tran, T.T.; Elbadawi, C.; Lobo, C.; Wang, X.; Juodkazis, S.; Seniutinas, G.; Toth, M.; Aharonovich, I. Engineering and localization of quantum emitters in large hexagonal boron nitride layers. *ACS Appl. Mater. Interfaces* **2016**, *8*, 29642–29648. [CrossRef] [PubMed]
105. Lyu, C.; Zhu, Y.; Gu, P.; Qiao, J.; Watanabe, K.; Taniguchi, T.; Ye, Y. Single-photon emission from two-dimensional hexagonal boron nitride annealed in a carbon-rich environment. *Appl. Phys. Lett.* **2020**, *117*, 244002. [CrossRef]
106. Fischer, M.; Caridad, J.M.; Sajid, A.; Ghaderzadeh, S.; Ghorbani-Asl, M.; Gammelgaard, L.; Bøggild, P.; Thygesen, K.S.; Krasheninnikov, A.V.; Xiao, S.; et al. Controlled generation of luminescent centers in hexagonal boron nitride by irradiation engineering. *Sci. Adv.* **2021**, *7*, eabe7138. [CrossRef]
107. Chen, Y.; Li, C.; White, S.; Nonahal, M.; Xu, Z.Q.; Watanabe, K.; Taniguchi, T.; Toth, M.; Tran, T.T.; Aharonovich, I. Generation of high-density quantum emitters in high-quality, exfoliated hexagonal boron nitride. *ACS Appl. Mater. Interfaces* **2021**, *13*, 47283–47292. [CrossRef]
108. Chen, Y.; Gale, A.; Yamamura, K.; Horder, J.; Condos, A.; Watanabe, K.; Taniguchi, T.; Toth, M.; Aharonovich, I. Annealing of blue quantum emitters in carbon-doped hexagonal boron nitride. *Appl. Phys. Lett.* **2023**, *123*, 041902. [CrossRef]
109. Guo, N.J.; Liu, W.; Li, Z.P.; Yang, Y.Z.; Yu, S.; Meng, Y.; Wang, Z.A.; Zeng, X.D.; Yan, F.F.; Li, Q.; et al. Generation of spin defects by ion implantation in hexagonal boron nitride. *ACS Omega* **2022**, *7*, 1733–1739. [CrossRef]
110. Chejanovsky, N.; Rezai, M.; Paolucci, F.; Kim, Y.; Rendler, T.; Rouabeh, W.; Fávaro de Oliveira, F.; Herlinger, P.; Denisenko, A.; Yang, S.; et al. Structural attributes and photodynamics of visible spectrum quantum emitters in hexagonal boron nitride. *Nano Lett.* **2016**, *16*, 7037–7045. [CrossRef]
111. Fournier, C.; Plaud, A.; Roux, S.; Pierret, A.; Rosticher, M.; Watanabe, K.; Taniguchi, T.; Buil, S.; Quélin, X.; Barjon, J.; et al. Position-controlled quantum emitters with reproducible emission wavelength in hexagonal boron nitride. *Nat. Commun.* **2021**, *12*, 3779. [CrossRef] [PubMed]
112. Zabelotsky, T.; Singh, S.; Haim, G.; Malkinson, R.; Kadkhodazadeh, S.; Radko, I.P.; Aharonovich, I.; Steinberg, H.; Berg-Sørensen, K.; Huck, A.; et al. Creation of boron vacancies in hexagonal boron nitride exfoliated from bulk crystals for quantum sensing. *ACS Appl. Nano Mater.* **2023**, *6*, 21671–21678. [CrossRef] [PubMed]
113. Cun, H.; Iannuzzi, M.; Hemmi, A.; Roth, S.; Osterwalder, J.; Greber, T. Immobilizing individual atoms beneath a corrugated single layer of boron nitride. *Nano Lett.* **2013**, *13*, 2098–2103. [CrossRef] [PubMed]
114. Cun, H.; Hemmi, A.; Miniussi, E.; Bernard, C.; Probst, B.; Liu, K.; Alexander, D.T.; Kleibert, A.; Mette, G.; Weinl, M.; et al. Centimeter-sized single-orientation monolayer hexagonal boron nitride with or without nanovoids. *Nano Lett.* **2018**, *18*, 1205–1212. [CrossRef] [PubMed]
115. Kianinia, M.; White, S.; Froch, J.E.; Bradac, C.; Aharonovich, I. Generation of spin defects in hexagonal boron nitride. *ACS Photonics* **2020**, *7*, 2147–2152. [CrossRef]
116. Ziegler, J.; Klaiss, R.; Blaikie, A.; Miller, D.; Horowitz, V.R.; Alemán, B.J. Deterministic quantum emitter formation in hexagonal boron nitride via controlled edge creation. *Nano Lett.* **2019**, *19*, 2121–2127. [CrossRef] [PubMed]
117. Venturi, G.; Chiodini, S.; Melchioni, N.; Janzen, E.; Edgar, J.H.; Ronning, C.; Ambrosio, A. Selective Generation of Luminescent Defects in Hexagonal Boron Nitride. *Laser Photonics Rev.* **2024**, Volume 18, 2300973. [CrossRef]
118. Glushkov, E.; Macha, M.; Rath, E.; Navikas, V.; Ronceray, N.; Cheon, C.Y.; Ahmed, A.; Avsar, A.; Watanabe, K.; Taniguchi, T.; et al. Engineering optically active defects in hexagonal boron nitride using focused ion beam and water. *ACS Nano* **2022**, *16*, 3695–3703. [CrossRef]
119. Ngoc My Duong, H.; Nguyen, M.A.P.; Kianinia, M.; Ohshima, T.; Abe, H.; Watanabe, K.; Taniguchi, T.; Edgar, J.H.; Aharonovich, I.; Toth, M. Effects of high-energy electron irradiation on quantum emitters in hexagonal boron nitride. *ACS Appl. Mater. Interfaces* **2018**, *10*, 24886–24891. [CrossRef] [PubMed]
120. Gale, A.; Li, C.; Chen, Y.; Watanabe, K.; Taniguchi, T.; Aharonovich, I.; Toth, M. Site-specific fabrication of blue quantum emitters in hexagonal boron nitride. *ACS Photonics* **2022**, *9*, 2170–2177. [CrossRef]
121. Murzakhanov, F.F.; Yavkin, B.V.; Mamin, G.V.; Orlinskii, S.B.; Mumdzhi, I.E.; Gracheva, I.N.; Gabbasov, B.F.; Smirnov, A.N.; Davydov, V.Y.; Soltamov, V.A. Creation of negatively charged boron vacancies in hexagonal boron nitride crystal by electron irradiation and mechanism of inhomogeneous broadening of boron vacancy-related spin resonance lines. *Nanomaterials* **2021**, *11*, 1373. [CrossRef]

122. Yang, Y.Z.; Zhu, T.X.; Li, Z.P.; Zeng, X.D.; Guo, N.J.; Yu, S.; Meng, Y.; Wang, Z.A.; Xie, L.K.; Zhou, Z.Q.; et al. Laser direct writing of visible spin defects in hexagonal boron nitride for applications in spin-based technologies. *ACS Appl. Nano Mater.* **2023**, *6*, 6407–6414. [CrossRef]
123. Gan, L.; Zhang, D.; Zhang, R.; Zhang, Q.; Sun, H.; Li, Y.; Ning, C.Z. Large-scale, high-yield laser fabrication of bright and pure single-photon emitters at room temperature in hexagonal boron nitride. *ACS Nano* **2022**, *16*, 14254–14261. [CrossRef]
124. Hou, S.; Birowosuto, M.D.; Umar, S.; Anicet, M.A.; Tay, R.Y.; Coquet, P.; Tay, B.K.; Wang, H.; Teo, E.H.T. Localized emission from laser-irradiated defects in 2D hexagonal boron nitride. *2D Mater.* **2017**, *5*, 015010. [CrossRef]
125. Gao, X.; Pandey, S.; Kianinia, M.; Ahn, J.; Ju, P.; Aharonovich, I.; Shivaram, N.; Li, T. Femtosecond laser writing of spin defects in hexagonal boron nitride. *ACS Photonics* **2021**, *8*, 994–1000. [CrossRef]
126. Gottscholl, A.; Kianinia, M.; Soltamov, V.; Orlinskii, S.; Mamin, G.; Bradac, C.; Kasper, C.; Krambrock, K.; Sperlich, A.; Toth, M.; et al. Initialization and read-out of intrinsic spin defects in a van der Waals crystal at room temperature. *Nat. Mater.* **2020**, *19*, 540–545. [CrossRef] [PubMed]
127. Vogl, T.; Campbell, G.; Buchler, B.C.; Lu, Y.; Lam, P.K. Fabrication and deterministic transfer of high-quality quantum emitters in hexagonal boron nitride. *ACS Photonics* **2018**, *5*, 2305–2312. [CrossRef]
128. Vogl, T.; Doherty, M.W.; Buchler, B.C.; Lu, Y.; Lam, P.K. Atomic localization of quantum emitters in multilayer hexagonal boron nitride. *Nanoscale* **2019**, *11*, 14362–14371. [CrossRef]
129. Stern, H.L.; Wang, R.; Fan, Y.; Mizuta, R.; Stewart, J.C.; Needham, L.M.; Roberts, T.D.; Wai, R.; Ginsberg, N.S.; Klenerman, D.; et al. Spectrally resolved photodynamics of individual emitters in large-area monolayers of hexagonal boron nitride. *ACS Nano* **2019**, *13*, 4538–4547. [CrossRef]
130. Mendelson, N.; Xu, Z.Q.; Tran, T.T.; Kianinia, M.; Scott, J.; Bradac, C.; Aharonovich, I.; Toth, M. Engineering and tuning of quantum emitters in few-layer hexagonal boron nitride. *ACS Nano* **2019**, *13*, 3132–3140. [CrossRef]
131. Mendelson, N.; Morales-Inostroza, L.; Li, C.; Ritika, R.; Nguyen, M.A.P.; Loyola-Echeverria, J.; Kim, S.; Götzinger, S.; Toth, M.; Aharonovich, I. Grain dependent growth of bright quantum emitters in hexagonal boron nitride. *Adv. Opt. Mater.* **2021**, *9*, 2001271. [CrossRef]
132. Abidi, I.H.; Mendelson, N.; Tran, T.T.; Tyagi, A.; Zhuang, M.; Weng, L.T.; Özyilmaz, B.; Aharonovich, I.; Toth, M.; Luo, Z. Selective defect formation in hexagonal boron nitride. *Adv. Opt. Mater.* **2019**, *7*, 1900397. [CrossRef]
133. Fernandes, J.; Queirós, T.; Rodrigues, J.; Nemala, S.S.; LaGrow, A.P.; Placidi, E.; Alpuim, P.; Nieder, J.B.; Capasso, A. Room-temperature emitters in wafer-scale few-layer hBN by atmospheric pressure CVD. *FlatChem* **2022**, *33*, 100366. [CrossRef]
134. Li, C.; Mendelson, N.; Ritika, R.; Chen, Y.; Xu, Z.Q.; Toth, M.; Aharonovich, I. Scalable and deterministic fabrication of quantum emitter arrays from hexagonal boron nitride. *Nano Lett.* **2021**, *21*, 3626–3632. [CrossRef]
135. Chen, X.; Yue, X.; Zhang, L.; Xu, X.; Liu, F.; Feng, M.; Hu, Z.; Yan, Y.; Scheuer, J.; Fu, X. Activated Single Photon Emitters And Enhanced Deep-Level Emissions in Hexagonal Boron Nitride Strain Crystal. *Adv. Funct. Mater.* **2024**, *34*, 2306128. [CrossRef]
136. Proscia, N.V.; Shotan, Z.; Jayakumar, H.; Reddy, P.; Cohen, C.; Dollar, M.; Alkauskas, A.; Doherty, M.; Meriles, C.A.; Menon, V.M. Near-deterministic activation of room-temperature quantum emitters in hexagonal boron nitride. *Optica* **2018**, *5*, 1128–1134. [CrossRef]
137. Mendelson, N.; Chugh, D.; Reimers, J.R.; Cheng, T.S.; Gottscholl, A.; Long, H.; Mellor, C.J.; Zettl, A.; Dyakonov, V.; Beton, P.H.; et al. Identifying carbon as the source of visible single-photon emission from hexagonal boron nitride. *Nat. Mater.* **2021**, *20*, 321–328. [CrossRef]
138. Xu, X.; Martin, Z.O.; Sychev, D.; Lagutchev, A.S.; Chen, Y.P.; Taniguchi, T.; Watanabe, K.; Shalaev, V.M.; Boltasseva, A. Creating quantum emitters in hexagonal boron nitride deterministically on chip-compatible substrates. *Nano Lett.* **2021**, *21*, 8182–8189. [CrossRef] [PubMed]
139. Perdew, J.P.; Chevary, J.A.; Vosko, S.H.; Jackson, K.A.; Pederson, M.R.; Singh, D.J.; Fiolhais, C. Atoms, molecules, solids, and surfaces: Applications of the generalized gradient approximation for exchange and correlation. *Phys. Rev. B* **1992**, *46*, 6671. [CrossRef]
140. Heyd, J.; Scuseria, G.E.; Ernzerhof, M. Hybrid functionals based on a screened Coulomb potential. *J. Chem. Phys.* **2003**, *118*, 8207–8215. [CrossRef]
141. Tawfik, S.A.; Ali, S.; Fronzi, M.; Kianinia, M.; Tran, T.T.; Stampfl, C.; Aharonovich, I.; Toth, M.; Ford, M.J. First-principles investigation of quantum emission from hBN defects. *Nanoscale* **2017**, *9*, 13575–13582. [CrossRef]
142. Hamdi, H.; Thiering, G.; Bodrog, Z.; Ivády, V.; Gali, A. Stone–Wales defects in hexagonal boron nitride as ultraviolet emitters. *npj Comput. Mater.* **2020**, *6*, 178. [CrossRef]
143. Zhang, Y.; Cheng, G.; Peng, W.; Tang, Z. Spintronic and electronic properties of a positively charged NBVN center in hexagonal boron nitride monolayer. *Comput. Mater. Sci.* **2014**, *95*, 316–319. [CrossRef]
144. Noh, G.; Choi, D.; Kim, J.H.; Im, D.G.; Kim, Y.H.; Seo, H.; Lee, J. Stark tuning of single-photon emitters in hexagonal boron nitride. *Nano Lett.* **2018**, *18*, 4710–4715. [CrossRef] [PubMed]
145. Abdi, M.; Chou, J.P.; Gali, A.; Plenio, M.B. Color Centers in Hexagonal Boron Nitride Monolayers: A Group Theory and Ab Initio Analysis. *ACS Photonics* **2018**, *5*, 1967–1976. [CrossRef]
146. Wu, F.; Galatas, A.; Sundararaman, R.; Rocca, D.; Ping, Y. First-principles engineering of charged defects for two-dimensional quantum technologies. *Phys. Rev. Mater.* **2017**, *1*, 071001. [CrossRef]

147. Sajid, A.; Thygesen, K.S. VNCB defect as source of single photon emission from hexagonal boron nitride. *2D Mater.* **2020**, *7*, 031007. [CrossRef]
148. Sajid, A.; Reimers, J.R.; Ford, M.J. Defect states in hexagonal boron nitride: Assignments of observed properties and prediction of properties relevant to quantum computation. *Phys. Rev. B* **2018**, *97*, 064101. [CrossRef]
149. Linderälv, C.; Wieczorek, W.; Erhart, P. Vibrational signatures for the identification of single-photon emitters in hexagonal boron nitride. *Phys. Rev. B* **2021**, *103*, 115421. [CrossRef]
150. Wang, R.; Yang, J.; Wu, X.; Wang, S. Local charge states in hexagonal boron nitride with Stone–Wales defects. *Nanoscale* **2016**, *8*, 8210–8219. [CrossRef] [PubMed]
151. Museur, L.; Feldbach, E.; Kanaev, A. Defect-related photoluminescence of hexagonal boron nitride. *Phys. Rev. B—Condens. Matter Mater. Phys.* **2008**, *78*, 155204. [CrossRef]
152. Vokhmintsev, A.; Weinstein, I.; Zamyatin, D. Electron-phonon interactions in subband excited photoluminescence of hexagonal boron nitride. *J. Lumin.* **2019**, *208*, 363–370. [CrossRef]
153. Uddin, M.; Li, J.; Lin, J.; Jiang, H. Probing carbon impurities in hexagonal boron nitride epilayers. *Appl. Phys. Lett.* **2017**, *110*, 182107. [CrossRef]
154. Era, K.; Minami, F.; Kuzuba, T. Fast luminescence from carbon-related defects of hexagonal boron nitride. *J. Lumin.* **1981**, *24*, 71–74. [CrossRef]
155. Mackoit-Sinkevičienė, M.; Maciaszek, M.; Van de Walle, C.G.; Alkauskas, A. Carbon dimer defect as a source of the 4.1 eV luminescence in hexagonal boron nitride. *Appl. Phys. Lett.* **2019**, *115*, 212101. [CrossRef]
156. Winter, M.; Bousquet, M.H.; Jacquemin, D.; Duchemin, I.; Blase, X. Photoluminescent properties of the carbon-dimer defect in hexagonal boron-nitride: A many-body finite-size cluster approach. *Phys. Rev. Mater.* **2021**, *5*, 095201. [CrossRef]
157. Huang, P.; Grzeszczyk, M.; Vaklinova, K.; Watanabe, K.; Taniguchi, T.; Novoselov, K.; Koperski, M. Carbon and vacancy centers in hexagonal boron nitride. *Phys. Rev. B* **2022**, *106*, 014107. [CrossRef]
158. Jara, C.; Rauch, T.; Botti, S.; Marques, M.A.; Norambuena, A.; Coto, R.; Castellanos-Águila, J.; Maze, J.R.; Munoz, F. First-principles identification of single photon emitters based on carbon clusters in hexagonal boron nitride. *J. Phys. Chem. A* **2021**, *125*, 1325–1335. [CrossRef]
159. Golami, O.; Sharman, K.; Ghobadi, R.; Wein, S.C.; Zadeh-Haghighi, H.; Gomes da Rocha, C.; Salahub, D.R.; Simon, C. A b initio and group theoretical study of properties of a carbon trimer defect in hexagonal boron nitride. *Phys. Rev. B* **2022**, *105*, 184101. [CrossRef]
160. Auburger, P.; Gali, A. Towards ab initio identification of paramagnetic substitutional carbon defects in hexagonal boron nitride acting as quantum bits. *Phys. Rev. B* **2021**, *104*, 075410. [CrossRef]
161. Huang, B.; Lee, H. Defect and impurity properties of hexagonal boron nitride: A first-principles calculation. *Phys. Rev. B—Condens. Matter Mater. Phys.* **2012**, *86*, 245406. [CrossRef]
162. Weston, L.; Wickramaratne, D.; Mackoit, M.; Alkauskas, A.; Van de Walle, C.G. Native point defects and impurities in hexagonal boron nitride. *Phys. Rev. B* **2018**, *97*, 214104. [CrossRef]
163. Liu, X.; Gao, Z.; Wang, V.; Luo, Z.; Lv, B.; Ding, Z.; Zhang, Z. Extrapolated defect transition level in two-dimensional materials: the case of charged native point defects in monolayer hexagonal boron nitride. *ACS Appl. Mater. Interfaces* **2020**, *12*, 17055–17061. [CrossRef] [PubMed]
164. Ivády, V.; Barcza, G.; Thiering, G.; Li, S.; Hamdi, H.; Chou, J.P.; Legeza, Ö.; Gali, A. Ab initio theory of the negatively charged boron vacancy qubit in hexagonal boron nitride. *npj Comput. Mater.* **2020**, *6*, 41. [CrossRef]
165. Xia, Y.; Li, Q.; Kim, J.; Bao, W.; Gong, C.; Yang, S.; Wang, Y.; Zhang, X. Room-temperature giant Stark effect of single photon emitter in van der Waals material. *Nano Lett.* **2019**, *19*, 7100–7105. [CrossRef] [PubMed]
166. Scavuzzo, A.; Mangel, S.; Park, J.H.; Lee, S.; Loc Duong, D.; Strelow, C.; Mews, A.; Burghard, M.; Kern, K. Electrically tunable quantum emitters in an ultrathin graphene–hexagonal boron nitride van der Waals heterostructure. *Appl. Phys. Lett.* **2019**, *114*, 062104. [CrossRef]
167. Akbari, H.; Biswas, S.; Jha, P.K.; Wong, J.; Vest, B.; Atwater, H.A. Lifetime-limited and tunable quantum light emission in h-BN via electric field modulation. *Nano Lett.* **2022**, *22*, 7798–7803. [CrossRef]
168. Zhigulin, I.; Horder, J.; Ivády, V.; White, S.J.; Gale, A.; Li, C.; Lobo, C.J.; Toth, M.; Aharonovich, I.; Kianinia, M. Stark effect of blue quantum emitters in hexagonal boron nitride. *Phys. Rev. Appl.* **2023**, *19*, 044011. [CrossRef]
169. Xu, Z.Q.; Mendelson, N.; Scott, J.A.; Li, C.; Abidi, I.H.; Liu, H.; Luo, Z.; Aharonovich, I.; Toth, M. Charge and energy transfer of quantum emitters in 2D heterostructures. *2D Mater.* **2020**, *7*, 031001. [CrossRef]
170. Prasad, M.K.; Al-Ani, O.A.; Goss, J.P.; Mar, J.D. Charge transfer due to defects in hexagonal boron nitride/graphene heterostructures: An ab initio study. *Phys. Rev. Mater.* **2023**, *7*, 094003. [CrossRef]
171. Yu, M.; Yim, D.; Seo, H.; Lee, J. Electrical charge control of h-BN single photon sources. *2D Mater.* **2022**, *9*, 035020. [CrossRef]
172. White, S.J.; Yang, T.; Dontschuk, N.; Li, C.; Xu, Z.Q.; Kianinia, M.; Stacey, A.; Toth, M.; Aharonovich, I. Electrical control of quantum emitters in a Van der Waals heterostructure. *Light Sci. Appl.* **2022**, *11*, 186. [CrossRef] [PubMed]
173. Elshaari, A.W.; Skalli, A.; Gyger, S.; Nurizzo, M.; Schweickert, L.; Esmaeil Zadeh, I.; Svedendahl, M.; Steinhauer, S.; Zwiller, V. Deterministic integration of hBN emitter in silicon nitride photonic waveguide. *Adv. Quantum Technol.* **2021**, *4*, 2100032. [CrossRef]

174. Kim, S.; Duong, N.M.H.; Nguyen, M.; Lu, T.J.; Kianinia, M.; Mendelson, N.; Solntsev, A.; Bradac, C.; Englund, D.R.; Aharonovich, I. Integrated on chip platform with quantum emitters in layered materials. *Adv. Opt. Mater.* **2019**, *7*, 1901132. [CrossRef]
175. Li, C.; Froch, J.E.; Nonahal, M.; Tran, T.N.; Toth, M.; Kim, S.; Aharonovich, I. Integration of hBN quantum emitters in monolithically fabricated waveguides. *ACS Photonics* **2021**, *8*, 2966–2972. [CrossRef]
176. Gérard, D.; Rosticher, M.; Watanabe, K.; Taniguchi, T.; Barjon, J.; Buil, S.; Hermier, J.P.; Delteil, A. Top-down integration of an hBN quantum emitter in a monolithic photonic waveguide. *Appl. Phys. Lett.* **2023**, *122*. [CrossRef]
177. Fröch, J.E.; Kim, S.; Mendelson, N.; Kianinia, M.; Toth, M.; Aharonovich, I. Coupling hexagonal boron nitride quantum emitters to photonic crystal cavities. *ACS Nano* **2020**, *14*, 7085–7091. [CrossRef]
178. Tran, T.T.; Wang, D.; Xu, Z.Q.; Yang, A.; Toth, M.; Odom, T.W.; Aharonovich, I. Deterministic coupling of quantum emitters in 2D materials to plasmonic nanocavity arrays. *Nano Lett.* **2017**, *17*, 2634–2639. [CrossRef] [PubMed]
179. Pela, R.R.; Hsiao, C.L.; Hultman, L.; Birch, J.; Gueorguiev, G.K. Electronic and optical properties of core-shell InAlN nanorods: A comparative study via LDA, LDA-1/2, mBJ, HSE06, G0W0 and BSE methods. *Phys. Chem. Chem. Phys. PCCP* **2024**, *26*, 7504–7514. [CrossRef]
180. Deshpande, S.; Frost, T.; Hazari, A.; Bhattacharya, P. Electrically pumped single-photon emission at room temperature from a single InGaN/GaN quantum dot. *Appl. Phys. Lett.* **2014**, *105*. [CrossRef]
181. Palacios-Berraquero, C.; Barbone, M.; Kara, D.M.; Chen, X.; Goykhman, I.; Yoon, D.; Ott, A.K.; Beitner, J.; Watanabe, K.; Taniguchi, T.; et al. Atomically thin quantum light-emitting diodes. *Nat. Commun.* **2016**, *7*, 71–89. [CrossRef]

Disclaimer/Publisher's Note: The statements, opinions and data contained in all publications are solely those of the individual author(s) and contributor(s) and not of MDPI and/or the editor(s). MDPI and/or the editor(s) disclaim responsibility for any injury to people or property resulting from any ideas, methods, instructions or products referred to in the content.